Applied Energy 388 (2025) 125628

Contents lists available at ScienceDirect

Applied Energy

journal homepage: www.elsevier.com/locate/apenergy

Design strategies for mainstream flow channels in large-area PEMFC: From typical units to large areas

Zhuo Zhang, Hong-Bing Quan, Sai-Jie Cai, Zheng-Dao Li, Wen-Quan Tao *

Key Laboratory of Thermo-Fluid Science & Engineering of MOE, Xi'an Jiaotong University, Xi'an, Shaanxi 710049, PR China

HIGHLIGHTS

- A systematic study was conducted on the PEMFC area magnification problem.
- A general calculation method of concentration loss is proposed.
- The mechanism of structural factors on specific voltage losses is deeply revealed.
- Among three area manification strategies, adding channel branches is suggested.

ARTICLE INFO

Keywords:
PEMFC
Area magnification
Pump loss
Voltage loss
Reactant concentration

ABSTRACT

Developing a large-scale flow field is essential for high-power proton exchange membrane fuel cells. A typical small-scale unit should be expanded to create the mainstream zone of a large-area flow field. This study investigated various design strategies for area magnification through numerical analysis. The impacts of channel length, number of channel branches, scaling factor, and channel/rib ratio on cell performance were thoroughly analyzed. An extraction method for concentration loss was devised to evaluate the primary voltage loss, and a contribution factor was determined. It was found that adding channel branches and proportional amplification led to a performance decline of 4.3 % and 42.6 %, respectively. However, extending channel length can slightly improve the PEMFC power density by 0.5 %–3.4 %. All three area magnification methods affect the bulk concentration in the channel, thereby influencing concentration loss. Moreover, proportional amplification and increasing C/R ratio can also deteriorate the mass transport ability from channel to porous electrode. When adjusting the channel length and C/R ratio, concentration loss is emerged as the primary factor driving performance differences, with a contribution factor exceeding 80 %, significantly higher than the other two voltage losses. However, in the case of altering the number of branches and proportional amplification, ohmic or activation loss also plays a crucial role. The performance of large-area fuel cells will be significantly improved if the area amplification strategy is selected reasonably. Among the three area magnification strategies, adding channel branches is suggested, considering both pump loss and performance degradation. For channel lengths exceeding 100 mm, the pump power density increased exponentially (more than eight times), which is unfavorable. Proportional amplification may lead to a substantial decline (>40 %) in cell output performance.

1. Introduction

Hydrogen is one of the earliest elements of the universe. Its abundance is high, comprising 75 % of the mass of universe. Hydrogen gas is a highly efficient, environmentally friendly, and clean energy source [1]. In the hydrogen energy systems, fuel cells become key equipment that convert the chemical energy of hydrogen into electricity [2]. Based on the type of electrolyte used, fuel cells can be categorized into alkaline fuel cells (AFCs), proton exchange membrane fuel cells (PEMFCs), phosphoric acid fuel cells (PAFCs), molten carbonate fuel cells (MCFCs), and solid oxide fuel cells (SOFCs) [3]. Among these, with the advantages of high energy density, high efficiency, low operating temperature, and quick start-up, PEMFC has become the most popular and promising power source [4].

Driven by market demand and technological advancements, high-power fuel cell products have become mainstream. In the field of transportation, heavy trucks are in urgent demand for applications in

---

* Corresponding author.
E-mail address: wqtao@mail.xjtu.edu.cn (W.-Q. Tao).

https://doi.org/10.1016/j.apenergy.2025.125628
Received 14 November 2024; Received in revised form 4 February 2025; Accepted 22 February 2025

Nomenclature

Latin symbols

a_{Pt}	activated surface area per volume of platinum particles ($\mathrm{m^{-1}}$)
A_{act}	active area ($\mathrm{m^2}$)
c	concentration($\mathrm{mol\cdot m^{-3}}$)
C_{p}	specific heat capacity($\mathrm{J\cdot kg^{-1}\cdot K^{-1}}$)
D	diffusivity($\mathrm{m^2\cdot s^{-1}}$)
E	voltage
EW	equivalent molecular weight of dry membrane ($\mathrm{kg\cdot kmol^{-1}}$)
F	Faraday's constant(96,485C$\cdot\mathrm{mol^{-1}}$)
I	current density($\mathrm{A\cdot m^{-2}}$)
j	reaction rate($\mathrm{A\cdot m^{-3}}$)
j_0	exchange current density($\mathrm{A\cdot m^{-3}}$)
K	intrinsic permeability($\mathrm{m^2}$)
k	thermal conductivity($\mathrm{W\cdot m^{-1}\cdot K^{-1}}$) or relative permeability
M	molar mass($\mathrm{kg\cdot kmol^{-1}}$)
n_{d}	electroosmotic drag coefficient
p	pressure(Pa)
q_{v}	volume flow rate($\mathrm{m^3\cdot s^{-1}}$)
R	gas constant($\mathrm{J\cdot mol^{-1}\cdot K^{-1}}$)
S	source term
s_{lq}	liquid saturation
T	temperature(K)
$\vec{u}$	velocity($\mathrm{m\cdot s^{-1}}$)
V	voltage (V)
Y	mass fraction

Greek letters

ε	porosity
δ	thickness(m)
ρ	density($\mathrm{kg\cdot m^{-3}}$)
μ	dynamic viscosity(Pa·s)
κ	electrical conductivity($\mathrm{S\cdot m^{-1}}$)
ξ	compressor efficiency
γ'	γ phase change rate($\mathrm{s^{-1}}$)
η	overpotential or voltage loss(V)
θ	coverage raio
ϕ	potential(V)
λ	membrane water content
ω	contribution factor or energy parameters for the Temkin isothermal model

Subscripts and superscripts

a	anode
act	activation
bulk	bulk value
con	concentration
c	cathode
eff	effective value
ele	electronic
eq	equilibrium water content
E	energy
g	gas
i	certain gas species
in	inlet
ion	proton
l,lq	liquid water
lh	latent heat
m	mass
mw	membrane water
mem	membrane
O	original
ohm	ohmic
out	output
over	overpotential
R	revised
rev	reversible
ref	reference
sat	saturation
u	velocity
v-l	vapor to liquid
v-m	vapor to membrane water (vice verse)
vp	water vapor
0	atmosphere parameter

Abbreviations

ACL	anode catalyst layer
AFC	alkaline fuel cell
BP	bipolar plate
B-V	Butler-Volmer
CCL	cathode catalyst layer
CCM	catalyst-coated membrane
CFD	computational fluid dynamic
CGDL	cathode gas diffusion layer
CL	catalyst layer
CMPL	cathode microporous layer
CRDZ	channel-ridge distribution zone
C/R	channel/rib
GC	gas channel
GDL	gas diffusion layer
DMDZ	dot matrix distribution zone
EIS	electrochemical impedance spectroscopy
FF	flow field
MCFC	molten carbonate fuel cell
MPL	microporous layer
PAFC	phosphoric acid fuel cell
PEM	proton exchange membrane
PEMFC	proton exchange membrane fuel cell
SOFC	solid oxide fuel cell
UDF	user defined function

high-power fuel cells (over 200 kW) [5]. As an important production tool, heavy trucks are often used in heavy-duty long-distance transportation, with characteristics such as long-term operation, high load rate, and continuous high-speed working conditions, all of which are in line with fuel cell power systems [6]. In addition to road transportation, fuel cell companies target areas such as ships, unmanned aerial vehicles, energy storage, industry, and buildings. Currently, ships suffer from high fuel consumption and emissions [7]. Replacing internal combustion engines with fuel cells is a favorable way to achieve carbon peak and carbon neutrality. Large ships have higher power requirements for fuel cells, and the continuous exploration of high-power fuel cell technology will lay the technical foundation for the development of hydrogen-powered ships. In addition, fuel cells play a key role in the energy storage field [8]. During the peak of variable renewable energy power generation, hydrogen can be stored by the electrolysis of water, and fuel cells (megawatt level) can be used to generate electricity during the power generation trough to help the peak regulation of electric networks [9]. In all these applications, it is necessary to develop high-power fuel cells.

1.1. Strategy for high-power PEMFC

To achieve a high-power output of a single fuel cell stack, there are two general methods: (1) connecting more cells in series and (2) improving the performance of a single cell. In many scenarios in which the volume is limited, increasing the number of cells is not recommended. Adding more cells causes difficulties in the stack assembly [10]. When the assembly force is uneven inside the cell stack, the middle of the cell stack is concave owing to insufficient clamping force [11]. Finall, an increase in the cell number leads to more severe voltage unevenness among different cells in the stack [12]. Therefore, maximizing the power generation of each cell as much as possible has become an effective method and research hotspot. This includes improving current density by optimizing each component of the fuel cell and expanding the active area to increase reaction sites.

A single fuel cell comprises anode and cathode bipolar plates (BPs), gas diffusion layers (GDLs), catalyst layers (CLs), and a proton exchange membrane sandwiched between the anode and cathode. Much work has been conducted to improve the current density by optimizing these components [13,14]. For example, Yin et al. [15] proposed a new elliptical groove gas diffusion layer to improve the transport properties. The results revealed that compared with the traditional GDL, the presence of an elliptical groove significantly accelerated the flow rate of the reactants and products. For the catalyst layer, Gao et al. [16] found that when the porosity of the CL was 0.6 and the average pore scale was between 40 and 140 nm, the fuel cell came to an optimal output performance. For the proton exchange membranes, Liu et al. [17] fabricated novel highly water-retentive PEMs using a strong magnetic field based on a new membrane formulation. It displayed efficient water absorption and retention at low relative humidity and elevated temperatures. In addition to membrane electrode assembly, the flow field plates are crucial components. Various novel structural designs have been introduced to enhance the performance. For example, 3D flow field (FF) including baffled FF [18], metal foam or porous FF [19], 3D wave FF [20], and 3D fine mesh FF [21] have been widely studied. Regarding traditional 2D FF, there are also many new designs, such as sinusoidal FF [22], biomimetic flow fields [23], partially narrow FF [24], 2D wave FF [25], and trap-shape FF [[26]. A detailed review can be found in our previous research [27]. Table I lists the relevant research on flow field plate design in recent years, all of which aimed to improve cell performance.

Expanding the active area is another simple but effective method of improving the power of a single cell. When the active area increases, both the flow field plate and membrane electrode need to be correspondingly increased. This introduces new problems in the design of fuel cell flow field plates. Wang et al. [28] pointed out that the cell voltage predicted by the full-scale model is significantly higher than conventional single-channel or no-dot-matrix models at high current density (>1.5 A·cm^{-2}). In other words, when the activation area increases, the cell performance changes accordingly. Therefore, in recent years, scholars have focused on the commercial level (large active area) in addition to the laboratory level (small active area). Many practical phenomena have been discovered in studies of large-area flow fields. For example, Zhang et al. [29] studied the reaction distribution in a commercial flow field (323 cm^2) comprising 63 channels in a PEMFC. The gas concentrations were found to be high in the channels near the edges.

A large-scale commercial flow field is composed of a distribution zone and a main stream zone (or reaction zone). Recent research on large-scale flow fields (including the above-mentioned studies) is summarized in Table I. On the one hand, with the increase in power and size in PEMFCs, the distributor is evolving as an important part of the flow field plates to facilitate uniform flow distributions and is gradually gaining more attention. Yu et al. [30] investigated the effect of the distribution zone design on the gas distribution uniformity and pressure drop. Relevant design criteria were proposed for the channel-ridge distribution zone (CRDZ) and dot matrix distribution zone (DMDZ). Lu

Table I
Flow field design.

Author and year	Active area	Focus point	Quantitative voltage loss analysis	Main outcomes
Zhang et al. [51] (2024)	5 cm^2	Porous flow field	Concentration loss	The limiting current density of porous FF increases by 49.9 % compared to channel-rib FF, significantly reducing mass transport losses.
Wu et al. [49] (2024)	245.76 cm^2	Partially narrow channels	All three	A partially narrowed flow field not only enhances the PEMFC net power density but also improves the drainage capacity.
Lu et al. [46] (2024)	303.85 cm^2	Distribution zone design	Ohmic loss	The new flow field design optimizes fuel cell secondary distribution under counter-flow intake, reduces pressure drop by 21 %, and increases net power by 8.1 %.
Liu et al. [48] (2024)	300 cm^2	Distribution zone design	All three	The forced shunt distribution zone and mixed-structure distribution zone enhance distribution uniformity are improved by 90.4 % and 55.5 %, respectively, compared to the dot-matrix distribution zone design.
Bulgarini et al. [52] (2024)	17.64 cm^2	Parallel/ Serpentine	No	The PtO$_x$ formation reduces fuel cell performance to up to 60 %–80 % when operating under high-voltage conditions.
Zheng et al. [18] (2024)	0.5 cm^2	Novel folded porous flow field	No	The folding rib structure in the new flow field design induces gas vortices within the channel, generates secondary flow, and improves the mass transfer capability of reactants.
Zou et al. [35] (2023)	25 cm^2	Optimized serpentine	No	An optimized flow field improves water drainage performance, increases fuel cell durability, and decelerates aging rates.

(continued on next page)

Table I (*continued*)

Author and year	Active area	Focus point	Quantitative voltage loss analysis	Main outcomes
Zhou et al. [22] (2023)	$< 5\ \text{cm}^2$	Sinusoidal wave flow fields	No	Opposite sinusoidal wave flow fields with single-inlet, dual-inlet, and block structures yield performance enhancements of 6.86 %, 1.26 %, and 2.31 %, respectively, compared with the parallel flow fields.
Zhang et al. [29] (2023)	323 cm^2	In-plane uniformity	No	The non-uniformity of cathode reactant distribution is generally higher than that of the anode, while temperature nonuniformity is lower along the flow direction.
Zhang et al. [27] (2023)	3.06 cm^2	Converging-diverging channel	No	Enhanced under-land cross flow and a higher effective mass transfer coefficient in the novel flow field improve reactant transport efficiency.
Zhang et al. [50] (2023)	Unknown	Cell structure and flow field type	All three	Fine channel/rib or porous flow-field designs significantly increase the power density
Yin et al. [53] (2023)	11.25 cm^2	Distribution zone design	No	Internal humidifying stack design is suitable for operations under dry reactants inflow conditions, providing enhanced performance and more uniform reactions.
Xie et al. [47] (2023)	310 cm^2	Water transition mechanism	Ohmic loss	Full-scale single-cell simulation domains are recommended as the primary approach for structural design, particularly under practical working conditions.
Wu et al. [54] (2023)	312 cm^2	Double cell structure	No	While the heat dissipation effect of the double-cell structure is less effective than the single-cell structure, their performances remain comparable.
Wang et al. [28] (2023)	366.6 cm^2	Physical quantity distribution	All three	Distribution zones effectively mitigate local oxygen starvation and water flooding, increasing PEMFC performance at high current density compared to conventional single-channel or non-dot-matrix models.
Wan et al. [55] (2023)	25 cm^2	Metal foam flow field	No	The height and width of metal foam have a pronounced effect on the temperature distribution in air-cooled PEMFCs.
He et al. [56] (2023)	113.92 cm^2	Physical quantity distribution	No	The gas distribution in the fluid flow is effectively optimized by the distribution zone, and the maximum concentration error of the anode is 4.87 %, which is significantly lower than that of the cathode.
Rahmani et al. [24] (2023)	2.5 cm^2	Raccoon channel flow field	No	The raccoon channel design increases output power by adjusting the amplitude or wavelength.
Park et al. [57] (2023)	40 cm^2	Metal foam flow field	No	Fuel cell performance improves by 14.67 % when a gas diffusion layer with high porosity and permeability is utilized.
Cai et al. [58] (2023)	1 cm^2	Baffled flow field	No	Ship-like baffles effectively push reactants downward and distribute them evenly, particularly in regions under the ribs.
Hao et al. [59] (2023)	0.72 cm^2	Trapezoidal tapering channel	No	An optimized PEMFC design improves the peak power by 8.5 % and extends the operating range of current density by 15.5 %.

et al. [31] proposed a distribution zone with a partially dotted matrix to further improve gas flow uniformity. The flow uniformity was maximized when the dotted matrix was placed near the gas inlet. Pan et al. [32] proposed a novel design for a combined distribution zone that incorporated central horizontal and lateral vertical meshes. A transverse-flow-control-based mechanism underlying flow distribution process was revealed. Through organized and detailed simulations, an optimum central porosity of 5 % and a lateral porosity of 76.7 % were determined.

The mainstream zone is the main area for expansion and typiccally includes interdigital, serpentine, and parallel flow fields. Min et al. [33] modified the channel layout of the serpentine flow field. It was found that the cell performance could be improved by increasing the segment number or channel path number in each segment. Santamaria et al. [34] studied the effect of the channel length of the interdigitated flow-field on the PEMFC performance. The results showed that a shorter channel interdigitated flow field could produce both higher maximum power and limiting current densities. Finally, the parallel flow field has been widely adopted owing to its lower pressure drop. As in the strategy adopted by Min et al. [33] and Santamaria et al. [34], there are two approaches corresponding to the two design parameters to realize the area magnification of the parallel flow field: (1) extending channel length and (2) adding more branches which means increasing channel numbers. Inspired by the scaling process, a third approach that simultaneously changes the length and width of the unit is also intuitive: (3) Proportional amplification. The three design methods for area magnification are shown in Fig. 1. As the active area of a high-power fuel cell increases, understanding how different area magnification methods affect the performance becomes increasingly important. Revealing the influence mechanism of area magnification on PEMFC performance can guide the design of large area flow field plates and promote the development of higher power fuel cells. However, there seems to be no such investigation in the literature in the past years. Most studies were conducted in fixed activation areas [36–38]. A design method for extending typical elements to large area flow field plates has not been reported. In Rocha et al.'s review of flow field plates [39], it was pointed out that the amplification behavior of MW-level PEMFC flow fields deserves further exploration.

1.2. PEMFC voltage analysis

As is well known, there are three performance losses in fuel cells: activation, ohmic, and concentration loss [40]. The smaller the values of these three losses, the better the cell performance. The activation loss reflects the catalyst activity, which is mainly determined by the intrinsic properties of the catalyst. After the catalyst was selected, the higher the bulk reactant concentration and temperature (the lower the production concentration at the same time), the lower the activation loss. The ohmic loss considers the voltage loss caused by charge (including electrons and protons) conduction inside the PEMFC. The concentration loss represents the voltage loss caused by the difference between the local and bulk concentrations of the reactants and products [41]. Through the EIS (Electrochemical Impedance Spectroscopy) method, the relative size of three voltage losses can be analyzed in an experiment test [42,43]. Nevertheless, analysis of the EIS data depends on the supposed equivalent circuit model, and an accurate voltage loss value cannot be obtained [44,45]. In contrast, a numerical simulation based on a three-dimensional multi-phase model is an effective way to study different voltage losses. As shown in Table I, most research did not perform a quantitative analysis of the effect of the flow field on the voltage loss. Lu et al. [46] elucidated the counter-flow mass transfer characteristics of a commercial large-scale PEMFC and Xie et al. [47] pointed out that a full-scale single-cell simulation domain should be the first choice for structural design. They only calculated the ohmic loss based on the electronic/proton potential from the PEMFC CFD (computational fluid dynamic) results. Although some researchers have analyzed all three voltage losses [28,48], details on how to obtain the concentration loss have not been provided. Wu et al. [49] and Zhang et al. [50] calculated the concentration loss using the following equations:

$$\eta_{\text{con}} = \frac{RT}{4F} ln\left(\frac{c_{\text{O}_2,\text{bulk}}}{c_{\text{O}_2,\text{CCL}}}\right) \tag{1}$$

where η_{con}(V) is concentration loss, R(J·mol^{-1}·K^{-1}) is gas constant, T(K) is local temperature, F(C·mol^{-1}) is Faraday's constant, $c_{\text{O}_2,\text{bulk}}$(mol·m^{-3}) and $c_{\text{O}_2,\text{CCL}}$ are bulk and local O_2 concentration, respectively.

Eq. (1) is derived from the simplified Butler-Volmer (B—V) equation, excluding the production accumulation effect in the CCL, originally the second term in the B—V equation. More intricate electrochemical models like the agglomerate model have formulas distinct from those of the B—V equations. Eq. (1) is inapplicable to these models owing to differing mass transfer resistance factors in the CCL. The electrochemical reaction rate formula of the agglomerate model is notably more intricate than that of the B—V equation. Hence, a new general method is urgently needed to determine the concentration loss from PEMFC CFD results. The treatment of ohmic loss is unequivocal. This study further refines the calculation of concentration loss based on the aforementioned research.

1.3. Existing challenges and shortcomings

The utilization of large-area flow field plates in high-power fuel cells is essential. Nevertheless, the design of the channels within this plates encounters various challenges. Desipite extensive research on innovative channel structures, the emphasis has been on local optimization. The design of large-area flow-field plates for achieving area magnification encounters a lack of defined criteria.

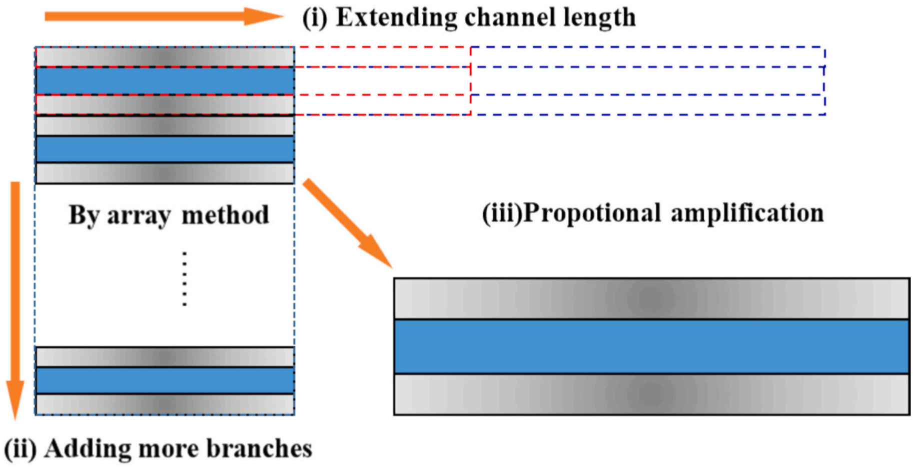

Fig. 1. Schematic of the three design methods of area magnification.

Almost all prior researches have been carried out in a specific active area. As shown in Table I, the active areas investigated in each study varied significantly, ranging from less than 1 cm^2 to over 300 cm^2. Most innovative structures have been examined using small-scale or laboratory-level PEMFC. The impact of the active area on cell performance remains uncertain. Comparing different flow field designs within the same activation area is not feasible, making it challenging to compare the results from different studies. The influence of changes in the active area and channel dimensions (following a similar pattern but with varying active areas) on cell performance has received limited attention. The performance variation of cells from a standard unit during the area-magnification process is not well understood.

Numerical simulations have been extensively used in the design of PEMFC flow fields; however, there is still a large room for improvement. The effect of flow field design on activation, ohmic, and concentration has been scarcely studied. The extraction methods for voltage loss, particularly concentration loss, require further elucidation and enhancement.

1.4. Main contents and innovations of the present study

This study analyzed three typical approaches for achieving area magnification. The structure pattern of typical units is preserved, while the effects of increasing length and width dimensions are examined. Eleven carefully designed cases were introduced (Section 2.1). First, in Sections 2.2 and 2.3, a three-dimensional (3D) multi-phase model is developed to investigate the performance variations under different design parameters. A general method for calculating concentration loss to extract and quantitatively analyze three types of voltage losses was proposed in Section 2.4. Section 2.5 analyzed factors influencing different voltage losses. Subsequently, using the developed model, simulations were conducted on the effects of channel length, number of channel branches, and scaling proportions on cell performance (Section 3.1–3.3). Comparative studies revealed mechanisms behind variations in different voltage losses. After determining extensions in both length and width, the aspect ratio of the channel/rib (C/R) of a typical unit was the remaining parameter. This study also investigated the C/R of typical units to provide a comprehensive flow-field design scheme, as detailed in Section 3.4. A more effective area-magnification strategy was proposed in Section 3.5 by comparing pump and PEMFC power densities. The impacts of changing four size design factors on the three voltage losses were summarized. Conclusions are presented in Section 4. This study aids in extending local structure design based on typical elements to large-area flow-field plates, laying a crucial foundation for large-area flow-field plate layout and expediting the commercialization of large-area high-power fuel cells. Moreover, the methodology presented in this paper can benefit the flat-plate flow field design of other types of fuel cells. This study can be used as a reference, and a corresponding model can be adopted to design the channel length, number of channel branches, scaling factor, and channel/rib ratio.

The innovation points of this study are concluded as follows:

1. A general method for calculating concentration loss is proposed. Using this method, all three voltage losses were extracted and analyzed.
2. The impact of four design factors in a large-scale flow field on cell performance is thoroughly compared, and a superior design approach is proposed; to the author's knowledge, this is the first study to conduct such an analysis in the relevant literature.
3. The contribution factor was determined to quantitatively study the three voltage losses. Thus, the mechanism by which different structural factors affect cell performance was revealed.

2. Methodology

2.1. Computational domain

To study the effects of the channel length, number of channel branches, scaling ratio, and C/R ratio on PEMFC performance, a total of 11 cases were establised. The key parameter configurations for each case are outlined in Table II. Both the anode and cathode followed the same flow pattern but in opposite directions. Cases I, II, III, and IV were utilized to assess the influence of channel length, as illustrated in Fig. 2(a). Initial investigations revealed a consistent enhancement in cell performance with longer flow channels. Notably, the current length of typical commercial flow-field plates does not exceed 500 mm, with the air pump power to PEMFC output power ratio already surpassing 7 % at this length. Consequently, channel lengths of 20/100/300/500 mm were selected. Fig. 2(b) displays the flow fields with three, six, and nine channel branches corresponding to Cases V, VI, and VII, respectively. Fig. 2(c) demonstrates uniform enlargement in the in-plane dimensions while maintaining consistent thickness in the through-plane direction. Building upon Case V, scaling factors of 1.5 and 2 were chosen to explore the impact of scaling ratio on PEMFC performance, leading to Cases VIII and IX, respectively. Regarding the C/R ratio, the total width of the channel and rib remain constant while their ratios were adjusted. Three C/R ratios (10:7, 1:1, and 7:10) were examined in Cases I, X, and XI as detailed in Table II. The specific geometric parameters are provided in Table III. This investigation concentrated on mainstream flow channels in large-area PEMFC systems. To enhance computational efficiency, simulations were conducted on a smaller fuel cell area. The trends and influencing mechanisms identified are applicable on a larger scale, offering insights for designing mainstream zones in large-scale flow fields.

2.2. 3D two-fluid PEMFC model

Cell performance is strongly linked to internal gas flow, water transport, charge conduction, and heat dissipation. A 3D two-fluid PEMFC model was created to analyze the impact of interconnected physical fields. The model was based on the subsequent fundamental assumptions:

1. The fuel cell attains stable operating conditions at a constant surface temperature [60].
2. The gas flow is laminar because of the low Reynolds number.
3. Both the gas species and gas mixture were treated as ideal gases.
4. When the assembly force was sufficient, the proportion of the contact resistance in the ohmic loss was much smaller than that in the mmebrane resistance. The contact resistance between different layers is ignored and this assumption is employed in many modeling works [46];
5. A low porosity of GDL (porosity $\varepsilon = 0.5$ [61]) is set to include the GDL compression effect, and ignore the uneven distribution of physical properties under the channel and rib [46,49]. This study

Table II
Case settings.

No	Channel branches	Channel length	C/R ratio	Scaling factor
I	Single channel	20 mm	10:7	O
II	Single channel	100 mm	10:7	O
III	Single channel	300 mm	10:7	O
IV	Single channel	500 mm	10:7	O
V	3 branches	20 mm	10:7	O
VI	6 branches	20 mm	10:7	O
VII	9 branches	20 mm	10:7	O
VIII	3 branches	30 mm	10:7	×1.5
IX	3 branches	40 mm	10:7	×2
X	Single channel	20 mm	1:1	O
XI	Single channel	20 mm	7:10	O

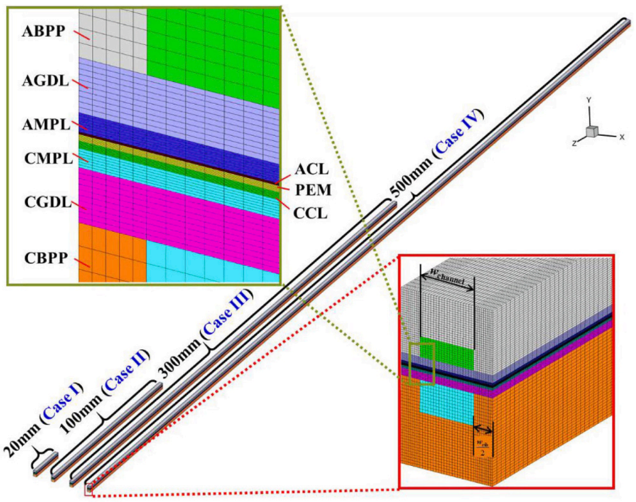

(a) Single channel

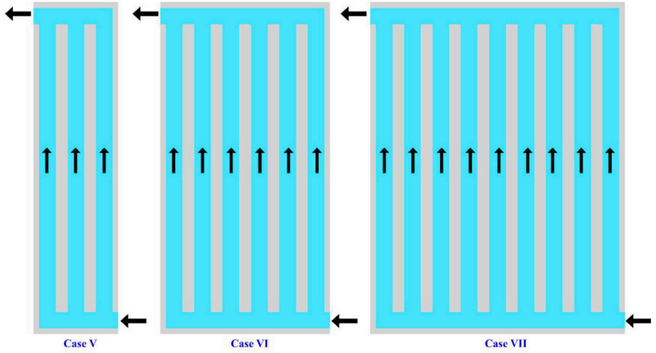

(b) Different bifuricates

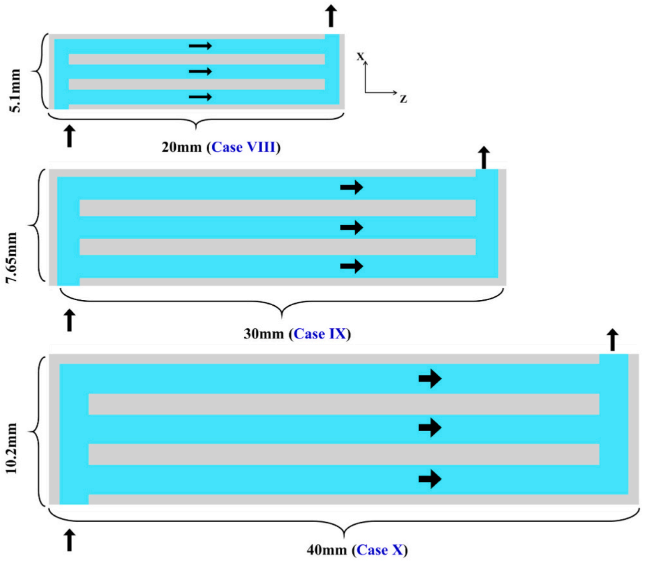

(c) Proportional amplification

Fig. 2. Schematic of the computational domain.

Table III
Key geometry parameters of the computational domain.

Parameters	Value
Depth of channel (mm)	0.35/0.55(anode/cathode)
Width of channel/rib (mm)	Case I: 1/0.7 Case X: 0.85/0.85 Case XI: 0.7/1
Bipolar plate length (mm)	20–500
Bipolar plate width (mm)	1.7–15.3
Thickness of GDL (μm)	130
Thickness of microporous layer (MPL) (μm)	45
Thickness of CL (μm)	6 /18 (anode/cathode)
Thickness of PEM (μm)	15

focuses on analyzing the change in mass transfer resistance caused by the change in the flow field. Thus, the relevant analysis is valid.

For the flow of the gaseous reactants and products, the continuity equation (Eq. (2)) and the momentum conservation equation (Eq. (3)) were adopted as follows

$$\nabla\cdot\left(\rho_g\vec{u}_g\right) = S_m \text{ (solved in GCs, MPLs, GDLs, CLs)} \tag{2}$$

$$\nabla\cdot\left(\frac{\rho_g\vec{u}_g\vec{u}_g}{\varepsilon^2(1-s_{lq})^2}\right) = -\nabla p_g + \mu_g\nabla\cdot\left(\nabla\left(\frac{\vec{u}_g}{\varepsilon(1-s_{lq})}\right)+\nabla\left(\frac{\vec{u}_g^{\,T}}{\varepsilon(1-s_{lq})}\right)\right) -\frac{2}{3}\mu_g\nabla\left(\nabla\cdot\left(\frac{\vec{u}_g}{\varepsilon(1-s_{lq})}\right)\right) + S_u \text{ (solved in GCs, MPLs, GDLs, CLs)} \tag{3}$$

where ρ_g(kg·m^{-3}) represents gas density, $\vec{u}_g$(m·s^{-1}) is gas velocity, ε is porosity, s_{lq} is liquid saturation, p_g(Pa) is gas pressure, μ_g(Pa·s) is gas dynamic viscosity. Mass transport involves convective and diffusion flux. Therefore, the species conservation equation for the *i*-species (*i*: H_2, O_2, water vapor) is described as follows

$$\nabla\cdot\left(\rho_g\vec{u}_gY_i\right) = \nabla\cdot\left(\rho_gD_i^{eff}\nabla Y_i\right) + S_i \quad \text{(solved in GCs, GDLs, MPLs, CLs)} \tag{4}$$

where Y_i is mass fraction, D_i^{eff}(m^2·s^{-1}) is effective diffusivity. In PEMFC, electrons are conducted in carbon-based solids, while protons are conducted in electrolytes in catalyst-coated membranes (CCMs). The governing equations for the electrons (Eq. (5)) and protons (Eq. (6)) are as follows:

$$0 = \nabla\cdot\left(\kappa_{ele}^{eff}\nabla\phi_{ele}\right) + S_{ele} \text{ (solved in BPs, GDLs, MPLs, CLs)} \tag{5}$$

$$0 = \nabla\cdot\left(\kappa_{ion}^{eff}\nabla\phi_{ion}\right) + S_{ion} \text{ (solved in PEM, CLs)} \tag{6}$$

where κ_{ele}^{eff} and κ_{ele}^{eff} (S·m^{-1}) are effective electron and proton conductivity, respectively; ϕ_{ele} and ϕ_{ele}(V) are effective electron and proton potential, respectively. Liquid water condenses from water vapor or through a reaction within the pores of the porous electrodes, satisfying the liquid pressure conservation equation:

$$0 = \nabla\cdot\left(\rho_l\frac{Kk_{lq}}{\mu_{lq}}\nabla p_{lq}\right) + S_{lq} \text{ (solved in GDLs, MPLs, CLs)} \tag{7}$$

where ρ_l(kg·m^{-3}) represents liquid density, K(m^2) denotes intrinsic permeability, k signifies permeability, μ_{lq}(Pa·s) stands for liquid dynamic viscosity, and p_{lq}(Pa) indicates liquid pressure. The CCM needs to maintain a certain degree of wettability to conduct protons. The conservation equation for dissolved water can be expressed as follows:

$$\nabla\cdot\left(\frac{n_d}{F}\nabla I_{ion}\right) = \frac{\rho_{mem}}{EW}\nabla\cdot\left(D_{mw}^{eff}\nabla\lambda_{\ mw}\right) + S_{mw} \text{ (solved in PEM, CLs)} \tag{8}$$

where n_d is the electroosmotic drag coefficient, I_{ion} (A·m^{-2}) represents the current density, ρ_{MEM} (kg·m^{-3}) denotes the membrane density, *EW* (kg·kmol^{-1}) stands for the equivalent molecular weight of the dry membrane, $D_{\mathrm{mw}}^{\mathrm{eff}}(\mathrm{m}^2\cdot\mathrm{s}^{-1})$ is effective membrane water diffusivity, and λ_{mw} signifies the membrane water content. The heat transfer and conversion processes were elucidated through the energy conservation equation:

$$\nabla\cdot\left(\left(\rho C_{\mathrm{p}}\vec{u}\right)^{\mathrm{eff}}T\right)=\nabla\cdot\left(k^{\mathrm{eff}}\nabla T\right)+S_{\mathrm{E}}\ (\text{solved in the whole domain}) \tag{9}$$

where $C_{\mathrm{p}}(\mathrm{J}\cdot\mathrm{kg}^{-1}\cdot\mathrm{K}^{-1})$ is specific heat capacity, and k^{eff} is effective thermal conductivity.

Detailed symbol definitions for the above equations are provided in Nomenclature. The calculation methods for the source terms that have a couple of different physical fields are listed in Table IV. The reaction rate (j_{a} ($\mathrm{A}\cdot\mathrm{m}^{-3}$) and j_{c}) that appeared in some source terms is calculated by the electrochemical model. Details of the electrochemical model are provided in the Supplementary Material. For further explanations or introductions to the model, please refer to our previous research [61].

In Table IV, M ($\mathrm{kg}\cdot\mathrm{kmol}^{-1}$) represents molar mass. γ' and γ (s^{-1}) denote phase change rates. δ_{PEM} (m), δ_{ACL} (m), and δ_{CCL} (m) indicate membrane thickness, anode catalyst layer thickness, and cathode catalyst layer thickness, respectively. ΔS ($\mathrm{J}\cdot\mathrm{kmol}^{-1}\cdot\mathrm{K}^{-1}$) stands for entropy production.

2.3. *Numerical implementation*

All geometric models introduced in Section 2.1 were imported into

Table IV
Source terms.

Source terms	Unit
Mass conservation equation: $S_{\mathrm{m}}=S_{\mathrm{H_2}}+S_{\mathrm{O_2}}+S_{\mathrm{vp}}(\text{all zones})$	$\mathrm{kg}\cdot\mathrm{m}^{-3}\cdot\mathrm{s}^{-1}$
Momentum conservation equation: $S_{\mathrm{u}}=\begin{cases}-\dfrac{\mu_{\mathrm{g}}}{K_{\mathrm{g}}}\vec{u}_{\mathrm{g}} & (\text{CLs, GDLs and GDLs})\\ 0 & (\text{other zones})\end{cases}$	$\mathrm{kg}\cdot\mathrm{m}^{-2}\cdot\mathrm{s}^{-2}$
Species conservation equation:	
$\mathrm{H_2}$: $S_{\mathrm{H_2}}=\begin{cases}-\dfrac{j_{\mathrm{a}}}{2F}M_{\mathrm{H_2}} & (\text{anode CL})\\ 0 & (\text{other zones})\end{cases}$	$\mathrm{kg}\cdot\mathrm{m}^{-3}\cdot\mathrm{s}^{-1}$
$\mathrm{O_2}$: $S_{\mathrm{O_2}}=\begin{cases}-\dfrac{j_{\mathrm{c}}}{4F}M_{\mathrm{O_2}} & (\text{cathode CL})\\ 0 & (\text{other zones})\end{cases}$	$\mathrm{kg}\cdot\mathrm{m}^{-3}\cdot\mathrm{s}^{-1}$
$\mathrm{H_2O}$: $S_{\mathrm{vp}}=\begin{cases}-S_{\mathrm{v-l}}+S_{\mathrm{v-m}}M_{\mathrm{H_2O}} & (\text{CLs})\\ -S_{\mathrm{v-l}} & (\text{MPLs, GDLs})\\ 0 & (\text{other zones})\end{cases}$	$\mathrm{kg}\cdot\mathrm{m}^{-3}\cdot\mathrm{s}^{-1}$
Condensation/evaporation: $S_{\mathrm{v-l}}=\begin{cases}\gamma\varepsilon(1-s_{\mathrm{lq}})(\rho_{\mathrm{vp}}-\rho_{\mathrm{sat}}), \rho_{\mathrm{vp}}>\rho_{\mathrm{sat}}\\ \gamma\varepsilon s_{\mathrm{lq}}(\rho_{\mathrm{vp}}-\rho_{\mathrm{sat}}), \rho_{\mathrm{vp}}<\rho_{\mathrm{sat}}\end{cases}$	$\mathrm{kg}\cdot\mathrm{m}^{-3}\cdot\mathrm{s}^{-1}$
Charge conservation equation:	
Electrons: $S_{\mathrm{ele}}=\begin{cases}-j_{\mathrm{a}} & (\text{anode CL})\\ j_{\mathrm{c}} & (\text{cathode CL})\\ 0 & (\text{other zones})\end{cases}$	$\mathrm{A}\cdot\mathrm{m}^{-3}$
Protons: $S_{\mathrm{ion}}=\begin{cases}j_{\mathrm{a}} & (\text{anode CL})\\ -j_{\mathrm{c}} & (\text{cathode CL})\\ 0 & (\text{other zones})\end{cases}$	$\mathrm{A}\cdot\mathrm{m}^{-3}$
Liquid pressure conservation equation: $S_{\mathrm{lq}}=\begin{cases}S_{\mathrm{v-l}} & (\text{anode CL, MPLs, GDLs})\\ \dfrac{j_{\mathrm{c}}}{2F}M_{\mathrm{H_2O}}+S_{\mathrm{v-l}} & (\text{cathode CL})\\ 0 & (\text{other zones})\end{cases}$	$\mathrm{kg}\cdot\mathrm{m}^{-3}\cdot\mathrm{s}^{-1}$
Membrane absorption and desorption: $S_{\mathrm{v\text{-}m}}=\dfrac{\rho_{\mathrm{mem}}}{EW}(\lambda_{\mathrm{mw}}-\lambda_{\mathrm{eq}})\gamma'$	$\mathrm{mol}\cdot\mathrm{m}^{-3}\cdot\mathrm{s}^{-1}$
Dissolved water conservation equation: $S_{\mathrm{mw}}=\begin{cases}-S_{\mathrm{v-m}}-\rho_{\mathrm{lq}}\dfrac{K_{\mathrm{PEM}}}{M_{\mathrm{H_2O}}\mu_{\mathrm{lq}}}\dfrac{p_{\mathrm{lq}}^{\mathrm{ACL}}-p_{\mathrm{lq}}^{\mathrm{CCL}}}{\delta_{\mathrm{PEM}}\delta_{\mathrm{ACL}}} & (\text{anode CL})\\ 0 & (\text{other zones})\\ -S_{\mathrm{v-m}}+\rho_{\mathrm{lq}}\dfrac{K_{\mathrm{PEM}}}{M_{\mathrm{H_2O}}\mu_{\mathrm{lq}}}\dfrac{p_{\mathrm{lq}}^{\mathrm{ACL}}-p_{\mathrm{lq}}^{\mathrm{CCL}}}{\delta_{\mathrm{PEM}}\delta_{\mathrm{CCL}}} & (\text{cathode CL})\end{cases}$	$\mathrm{mol}\cdot\mathrm{m}^{-3}\cdot\mathrm{s}^{-1}$
Energy conservation equation: $S_{\mathrm{E}}=\begin{cases}\dfrac{j_{\mathrm{a}}T\Delta S_{\mathrm{a}}}{4F}+j_{\mathrm{a}}\lvert\eta_{\mathrm{act}}\rvert+\lVert\nabla\phi_{\mathrm{ele}}\rVert^2\kappa_{\mathrm{ele}}^{\mathrm{eff}}+\lVert\nabla\phi_{\mathrm{ion}}\rVert^2\kappa_{\mathrm{ion}}^{\mathrm{eff}}+S_{\mathrm{lh}} & (\text{anode CL})\\ \dfrac{j_{\mathrm{c}}T\Delta S_{\mathrm{c}}}{4F}+j_{\mathrm{c}}\lvert\eta_{\mathrm{act}}\rvert+\lVert\nabla\phi_{\mathrm{ele}}\rVert^2\kappa_{\mathrm{ele}}^{\mathrm{eff}}+\lVert\nabla\phi_{\mathrm{ion}}\rVert^2\kappa_{\mathrm{ion}}^{\mathrm{eff}}+S_{\mathrm{lh}} & (\text{cathode CL})\\ \lVert\nabla\phi_{\mathrm{ele}}\rVert^2\kappa_{\mathrm{ele}}^{\mathrm{eff}}+S_{\mathrm{lh}} & (\text{GDL, MPL})\\ \lVert\nabla\phi_{\mathrm{ele}}\rVert^2\kappa_{\mathrm{ele}}^{\mathrm{eff}} & (\text{BP})\\ \lVert\nabla\phi_{\mathrm{ion}}\rVert^2\kappa_{\mathrm{ion}}^{\mathrm{eff}} & (\text{membrane})\\ 0 & (\text{other zones})\end{cases}$	$\mathrm{W}\cdot\mathrm{m}^{-3}$

ANSYS ICEM 2019 and discretized using a structured hexahedral mesh. The grid within the X-Y section was enlarged, as illustrated in Fig. 2(a). A grid-independence test was performed to enhance result reliability. As depicted in Fig. A1 in the Supplementary Material, for grid numbers exceeding 1.1 million, the average current density variation was less than 0.5 %. In the through-plane direction, PEM/CL/MPL/GDL/BP consisted of grids with 9/7/7/10/30 layers. Along the channel-length direction (*Z*-direction), the mesh density was 10 layers per millimeter, with higher density in the X-direction, as indicated in Fig. 2(a).

For boundary conditions, the anode and cathode inlet mass flow rate is calculated as follows:

$$m_a = \frac{\rho_a I \xi_a A_{act}}{2Fc_{inlet,H_2}} \tag{10}$$

$$m_c = \frac{\rho_c I \xi_c A_{act}}{4Fc_{inlet,O_2}} \tag{11}$$

where m (kg·s^{-1}) represents the inlet mass flow rate, ρ (kg·m^{-3}) is the gas mixture density, I (A·m^{-2}) denotes the average current density, ξ signifies the stoichiometric ratio, A (m^2) indicates the active area, F (C·mol^{-1}) is Faraday's constant, and c_{inlet} (mol·m^{-3}) denotes the inlet reactant gas concentration. Subscripts a and c correspond to the anode and cathode, respectively. The outlet pressure is maintained at 50 kPa. Further details regarding the experimental conditions are available in our previous study [14].

All the governing equations (Eq. (2) to Eq. (9)) were self-programmed using ANSYS FLUENT 2023 by User Defined Function (UDF). These equations were discretized by employing the finite-volume method. The second-order upwind scheme was utilized for the convection term and the central difference scheme for the diffusion term. The utilization of a UDF is essential for customizing and updating complex transport properties, source terms, and boundary conditions. Convergence was achieved when all residuals were less than 10^{-7}.

2.4. Experiment setup

To validate this model, experimental tests were performed using a specific fuel cell. A diagram of the test bench is illustrated in Fig. B1 in Appendix B. Each the anode and cathode are equipped with a flow control valve, humidifier, gas-heating apparatus, and gas-liquid separator. The fuel cell's temperature was regulated by an electric heating rod and a cooling fan.

The anode and cathode of the test cell consisted of single serpentine flow fields, each having an active area of 25 cm^2. Fig. 3(a) shows the computational domain established, maintaining geometric dimensions similar to an actual cell. The operating conditions pertinent to the experiments are detailed in Table V. Under each current, the relevant parameters exhibited stability for over 5 min before voltage measurement. A comparison between the experimental data and numerical simulation results is presented in Fig. 3(b), demonstrating a remarkable alignment between the two. The maximum error observed is less than 2 %.

2.5. Loss extraction method

Based on the reaction kinetics of fuel cells, the actual voltage of a fuel cell is lower than its reversible voltage. Therefore, the output voltage of the PEMFC can be calculated by subtracting the voltage drop from the thermodynamic voltage as follows:

$$V_{out} = E_{rev} - \eta_{act} - \eta_{ohm} - \eta_{con} \tag{12}$$

where E_{rev}(V) is thermodynamically predicted fuel cell voltage; η_{act}(V) is activation losses due to reaction kinetics; η_{ohm}(V) is ohmic losses from ionic and electronic conduction; η_{con}(V) is concentration losses due to mass transport. These voltage losses were derived from the simulation outcomes. The reversible voltage or open-circuit voltage was calculated using the Nernst Equation (Eq. (13)).

$$E_{rev} = 1.229 - 0.846 \times 10^{-3}(T - 298.15) + \frac{RT}{2F}\left(ln\frac{p_{in,H_2}}{p_0} + \frac{1}{2}ln\frac{p_{in,O_2}}{p_0}\right) \tag{13}$$

where p_{in,H_2}(Pa) is the inlet hydrogen pressure, p_{in,O_2}(Pa) is the inlet hydrogen pressure, and p_0(Pa) is the standard atmospheric pressure.

Ohmic loss can be determined based on the average electron or proton potentials at the respective surface. For example, Fig. 4 shows the potential changes in the through-plane direction. Charge conduction

Table V
Operating condition.

Current density	St_a	St_c	Outlet pressure	Inlet temperature*	Relative humidity**
0.1 A·cm^{-2}	13.5	5	20 kPa	343.15 K	100 %
0.2 A·cm^{-2}	3.5	3	20 kPa		
0.3 A·cm^{-2}	1.5	2	30 kPa		
0.4 A·cm^{-2}	1.5	2	40 kPa		
0.5–2.2 A·cm^{-2}	1.5	2	40 kPa		

* The inlet temperature of the anode/cathode side and cell temperature are the same, $T_{a\_inlet} = T_{c\_inlet} = T_{cell} = 343.15$ K. **Relative humidity $RH_a = RH_c = 100$ %.

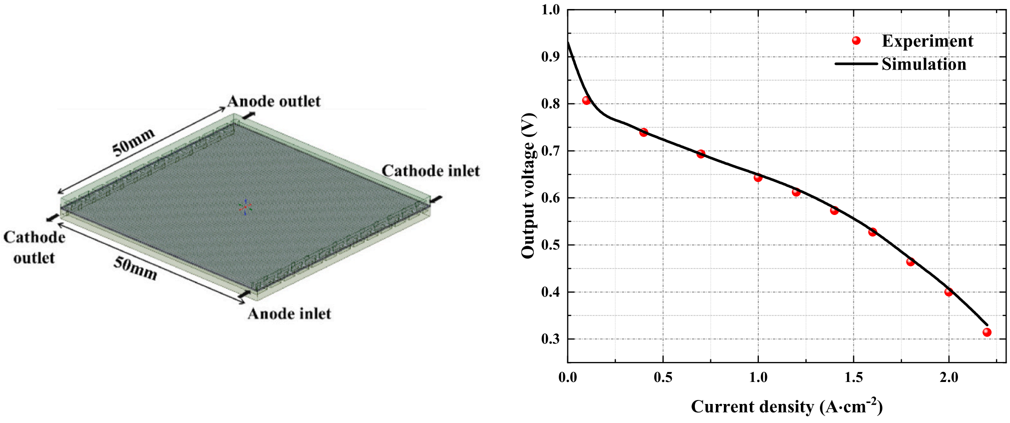

(a) Computational domain (b) Polarization curve

Fig. 3. Model validation.

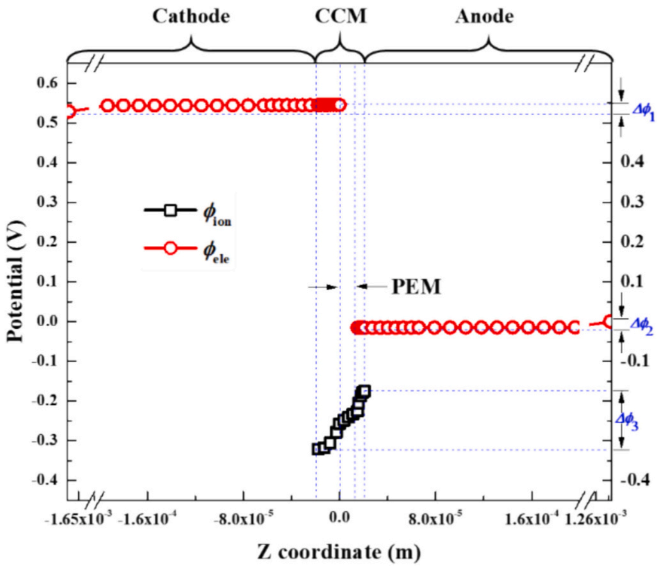

Fig. 4. Potential variations in the through-plane direction.

was defined by the corresponding electron (ϕ_{ele}) or ion (ϕ_{ion}) potentials in different regions. The ohmic loss (η_{ohm}) is calculated as follows:

$$\eta_{ohm} = \Delta\phi_1 + \Delta\phi_2 + \Delta\phi_3 \tag{14}$$

where $\Delta\phi_1$(V) and $\Delta\phi_2$(V) represent the ohmic losses of electron conduction at the anode and cathode, respectively, and $\Delta\phi_3$(V) is the ohmic loss of proton conduction in the catalyst-coated membrane.

In the catalyst layer, the local overpotential was determined by considering the local concentration of reactants/products and temperature. Consequently, the overpotential comprises activation and concentration losses. Calculating the concentration loss is a prerequisite for determining the activation loss.

In this study, the anode hydrogen supply was excessive with a stoichiometric ratio of 1.5. Moreover, the H_2 diffusivity is 3–5 times higher than that of O_2 [33,47]. As a result, even under high current density, the reactant concentration in the ACL did not significantly decrease compared to the channel, as illustrated in Fig. A2 in Supplementary Material. Simultaneously, the anode side exhibits high reaction activity, corresponding to a high exchange current density. Although the channel layout causes variations in local hydrogen distribution, the overall concentration loss at the anode is significantly less than that at the cathode. Therefore, the concentration loss on the anode side was disregarded, focusing soley on the cathode side. According to the formula of reaction rate in CCL (see Appendix), the cathode reaction rate j_c ($A\cdot m^{-3}$) is related to local liquid saturation (s_{lq}), O_2 concentration (c_{O_2}), temperature (T), and overpotential (η_{act}^{c}):

$$j_c = j_{0,c}^{ref}(1-s_{lq})a_{Pt}(1-\theta_{PtO})\frac{c_{O_2}^{Pt}}{c_{O_2}^{ref}}e^{\left(-\frac{F\alpha_c\eta_{act}^{c}}{RT}-\frac{\omega\theta_{PtO}}{RT}\right)} \tag{15}$$

where θ_{PtO} is the coverage ratio of PtO; a_{Pt} (m^{-1}) represents the activated surface area per volume of platinum particles; $c_{O_2}^{Pt}$ ($mol\cdot m^{-3}$) is the oxygen concentration near the platinum surface which is calculated from local oxygen concentration $c_{O_2,CCL}$ ($mol\cdot m^{-3}$); $c_{O_2}^{ref}$ ($mol\cdot m^{-3}$) is the reference concentration of oxygen; and ω is the energy parameters for the Temkin isothermal model. Eq. (15) reveals that for a catalyst with a specific activity determined by the intrinsic material characteristics, the higher the reaction rate, the higher the corresponding overpotential after the concentration and temperature of reactant/product are determined. Eq. (15) can be expressed in implicit function form as:

$$F\left(s_{lq}, c_{O_2}, \eta_{act}^{c}, T, j_c\right) = 0 \tag{16}$$

The local liquid saturation, O_2 concentration, temperature, reaction rate, and overpotential of each mesh were obtained from the numerical results. The concentration loss η_{con} represents the voltage drop due to the decrease in reactant concentration at the catalyst layer compared to the bulk concentration, and the increase in product concentration at the catalyst layer relative to the bulk concentration [62]. Firstly, retain T and j_c unchanged, replace the local $c_{O_2,CCL}$ with the bulk concentration, and replace the local liquid saturation with the bulk value. In this study, the average O_2 concentration in the cathode flow field is regarded as the bulk concentration ($c_{O_2\_bulk}$). Assuming rapid discharge of produced water, the bulk liquid saturation was set to 0. While the bulk value remained constant, the local concentrations within each mesh of the catalyst layer exhibited spatial variation. Therefore, gradients caused by uneven channel designs or variable flow rates of flow field has been considered. The distribution of concentration loss within the catalyst layer can be obtained, which means that the localized transport limitations can be considered. The final concentration loss is the average value in the catalytic layer. Subsequently solving Eq. (16) yields a new overpotential ($\eta_{over,R}^{c}$) corresponding to no mass transport loss. Finally, the concentration loss η_{con}(V):

$$\eta_{con} = \eta_{over,o}^{c} - \eta_{over,R}^{c} \tag{17}$$

The concentration loss calculation process is illustrated in Fig. 5. The activation loss η_{act} can be determined by reverse calculation from Eq. (18) once the reversible voltage E_{rev}(V), output voltage V_{out}(V), ohmic loss η_{ohm}(V), and concentration loss η_{con}(V) are all identified.

$$\eta_{act} = E_{rev} - V_{out} - \eta_{ohm} - \eta_{con} \tag{18}$$

2.6. *Loss analysis*

For ohmic loss, it can be seen from Fig. 4 that proton conduction loss accounts for the main part. The membrane conductivity or proton conductivity is highly related with membrane water content and temperature (See Fig. A3 in Supplementay Material). Temperature can indirectly impact the ohmic loss by influencing the membrane's water content. The higher the temperature, the lower the membrane water content. Essentially, the membrane water content will have a great effect on membrane conductivity and subsequently affects ohmic loss. Therefore, the ohmic loss and membrane water content variation under different design strategies shall be given.

The concentration loss represents the voltage loss caused by the mass transfer resistance of the flow field plate toward the reaction sites inside the porous electrode. By keeping the reaction rate (j_c) and temperature (T) constant and changing the concentrations of the reactants (c_{O_2}), the corresponding overpotential (η_{act}^{c}) can be obtained by solving Eq. (16). The effect of reactant concentration on the overpotential is shown in Fig. 6. It can be seen from Fig. 6 that the curve of the change in overpotential with concentration is downward convex.

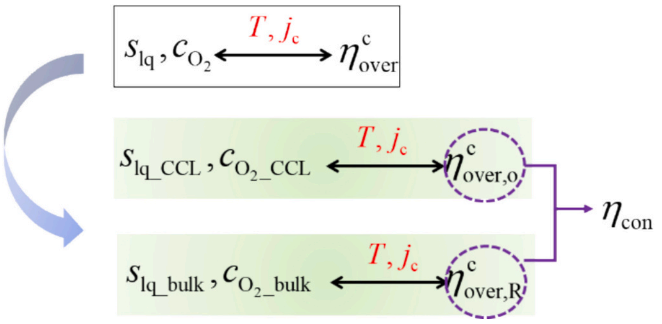

Fig. 5. Schematic diagram of concentration loss calculation process.

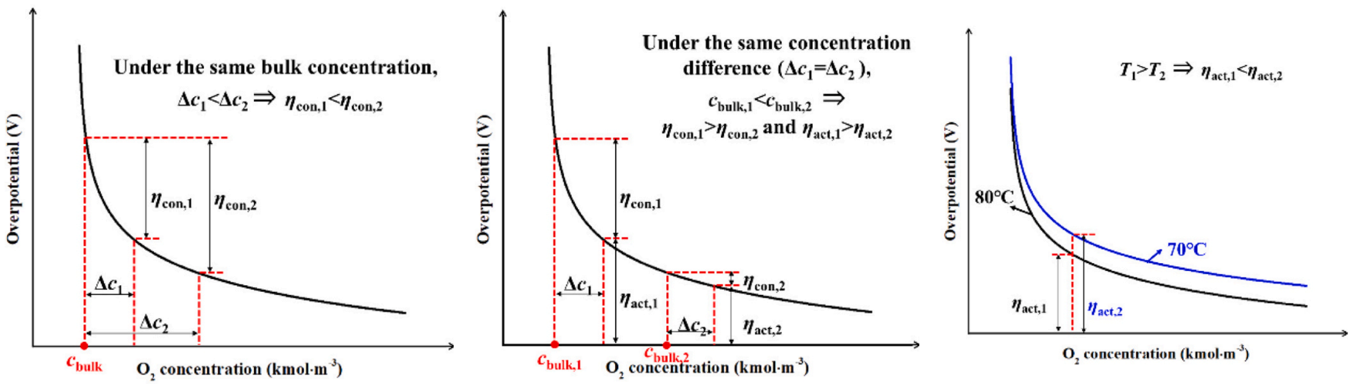

(a) Δc (b) Bulk O_2 concentration (c) Temperature

Fig. 6. Effect of reactant (O_2) concentration on overpotentials.

Owing to diffusion being the primary mode of reactant transport within PEMFC electrodes, the Δc can be used to characterize mass transport resistance. It is worth noting that temperature impacts the gas diffusion coefficient, and the Δc calculated here already incorporates this effect. Greater concentration differences result in increased concentration loss at equivalent bulk concentrations, as shown in Fig. 6(a). Both the concentration difference and the bulk concentration's absolute value can influence concentration loss. For a similar concentration difference ($\Delta c_1 = \Delta c_2$), higher bulk concentration values lead to reduced concentration loss, as depicted in Fig. 6(b).

The activation loss was influenced by the local temperature and the absolute values of the bulk concentration, after the intrinsic activity of the catalyst has been determined. For a consistent concentration difference ($\Delta c_1 = \Delta c_2$), higher bulk concentration values corresponded to lower activation losses, as shown in Fig. 6(b). Furthermore, maintaining a constant concentration while increasing the temperature resulted in a

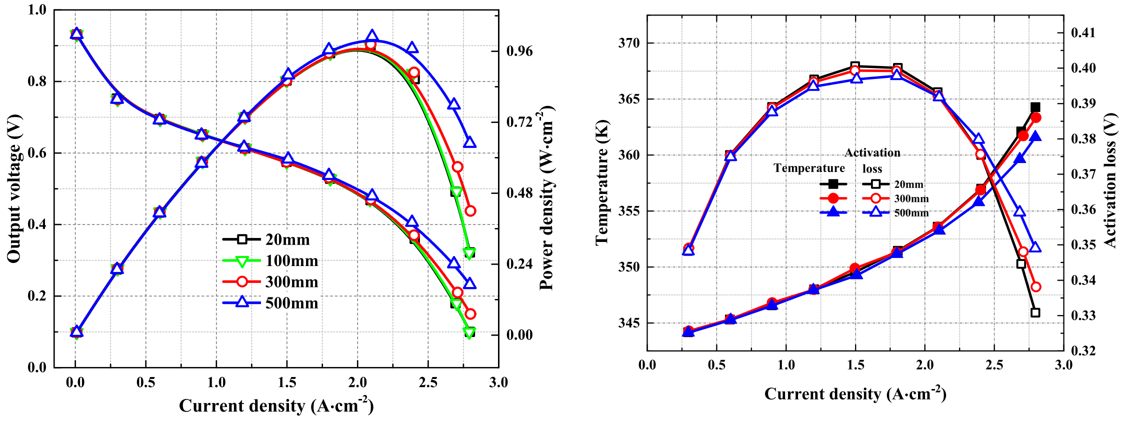

(a) Polarization and power density curve (b) Activation loss

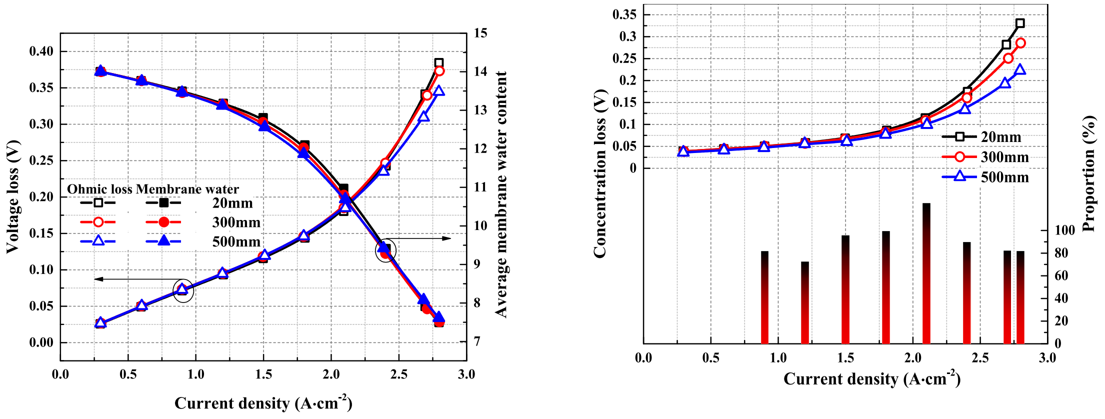

(c) Ohmic loss (d) Concentration loss

Fig. 7. Effect of channel length on the performance and voltage loss.

decrease in activation loss, as depicted in Fig. 6(c).

3. Results and discussion

In the present study, the effects of channel length, scaling factor, sub-channel number, and C/R ratio on cell performance are analyzed. The results of each independent factor analysis are given below, and then summarized and compared.

3.1. Effect of channel length

Four channel lengths, 20/100/300/500 mm are simulated in the present study. Fig. 7(a) illustrates the polarization curves and corresponding power density curves of a PEMFC with varying channel lengths. The cell performances at 20 mm and 100 mm were comparable. For simplicity, only the case with a 20 mm length is analyzed later. As the channel length increased, there was a significant improvement in performance, especially at high current densities. At a current density of 2.1 A·cm^{-2}, the cell power densities for 500 mm and 300 mm are 3.1 % and 0.5 % higher than that of 20 mm, respectively. To elucidate the performance difference mechanism, three voltage losses were extracted using the method outlined in Section 2.4.

The variation of average current density, temperature, and activation loss are shown in Fig. 7(b). The temperature gradually rises with increasing current density. At high current density, the temperature of the 20 mm cell with inferior electrical performance exceeds that of the 500 mm cell. The combined influence of current density (linked to the reaction rate) and temperature manifests as a peak resembling a mountain in the activation loss. Activation loss escalates with rising current density or reaction rate, while the higher temperature in the catalyst layer enhances the reference exchange current density, thereby reducing activation loss. At low currents, the reaction rate factor predominates, leading to increased activation loss with higher reaction. However, under high current, the temperature factor plays a dominant role. Elevated cell temperature boosts the reaction, resulting in a rapid decrease in activation loss. The activation peaks at 350–352 K for different channel lengths. In the 1.2–2.1 A·cm^{-2} range, the activation loss for the 20 mm channel is the highest due to the lowest bulk concentration of reactants in the channel, as elaborated later.

Fig. 7(c) shows the variation in ohmic loss, which is conistent across the three lengths. As the current density rises, the ohmic loss also increases gradually, and the growth rate is faster and faster. This phenomenon may be attributed to the rise in proton conduction resistance due to membrane water loss. The desorption of water from the membrane is evident at elevated temperatures, as indicated on the right axis in Fig. 7(c). The slight discrepancy at high current density can be attributed to variations in membrane water content. Furthermore, the membrane conductivity is shown in Fig. A4 in Supplymentay material. Its variation is highly similar to that of ohmic loss. Therefore, the ohmic loss curve can reflect the change of membrane conductivity. For brevity, only the change of ohmic loss is given later.

The concentration loss variation law is illustrated in Fig. 7(d). Significant differences in loss values for the three lengths were observed in the high current-density region. To quantify the impact of concentration loss on performance variation, the concentration loss contribution factor is defined as follows:

$$\omega = \left|\frac{\Delta\eta_{\text{con}}}{\Delta V_{\text{out}}}\right| = \left|\frac{\eta^1_{\text{con},i} - \eta^2_{\text{con},i}}{V^1_{\text{out},i} - V^2_{\text{out},i}}\right| \tag{19}$$

where $\eta_{\text{con},i}$ and $V_{\text{out},i}$ are the corresponding concentration losses and output voltages at the same current density, respectively. The superscripts 1 and 2 represent PEMFC with 20 mm and 500 mm channel lengths, respectively. Similarly, the proportion of activation and ohmic could be obtained by replacing $\Delta\eta_{\text{con}}$ with $\Delta\eta_{\text{act}}$ or $\Delta\eta_{\text{ohm}}$ in Eq. (19).

The histogram in Fig. 7(d) indicates that the concentration loss contribution rate is more than 80 %. This implies that concentration loss primarily accounted for the performance variation across varying channel lengths.

To further investigate the effect of channel length on concentration loss, Fig. 8 shows the average O_2 concentrations in the cathode side channel (CCH), gas diffusion layer (CGDL), cathode microporous layer (CMPL), and cathode catalyst layer (CCL) at 2.1 A·cm^{-2}. Comparing the oxygen concentration between the channel and catalyst layer reveals similar the mass transfer capacity or resistance ($\Delta c_1 = \Delta c_2 = \Delta c_3$). However, the concentration of reactants in the channel is higher when the channel is longer. As stated in Section 2.5, the absolute level of bulk concentration will also affect the concentration loss. This is the reason for the large concentration loss at 20 mm. This principle applies to activation loss as well.

The increase in bulk reactant concentration at different lengths is attributed to the rise in pressure. Under the same inlet cross-section, when the length of the channel increases by n times, the inlet flow velocity also increases by n times. Consequently, the pressure drop surged by almost n^2 times (inferred qualitatively from Weisbach's formula [62,63]). This indicates an elevated inlet pressure while keeping the outlet pressure constant. Finally, an increased inlet gas pressure led to a higher reactant concentration. The oxygen concentration fields in the cathode side channel and the porous electrode, corresponding to the three channel lengths, are shown in Figs. B2(a), (b), and (c) in Appendix B. To facilitate comparison, the various lengths were standardized and viewed from a unified perspective. As the flow channel length increased, the concentration near the entrance also increased, while the concentrations near the exit were similar for all three lengths.

The pressure drops in the anode and cathode channels are illustrated in Fig. B3 of Appendix B. At 2.1 A·cm^{-2}, the cathode side pressure drop for the 500 mm channel length is approximately 2.6 and 562 times greater than that of the 300 mm and 20 mm lengths, respectively. Given that the air compressor is the primary power-consuming component among the auxiliary parts of the fuel cell system, the ratio of air pump power to PEMFC output power was calculated. According to Fig. B3, for the 20 mm length, the air pump power can be disregarded. However, as the channel length exceeds 300 mm, the pump power proportion will increase to approximately 5 % at 2.8 A·cm^{-2}, which is deemed unacceptable.

3.2. Effect of branch number

Three branch numbers, 3/6/9 were simulated in the current study. Fig. 9 shows the PEMFC performance and voltage loss curves

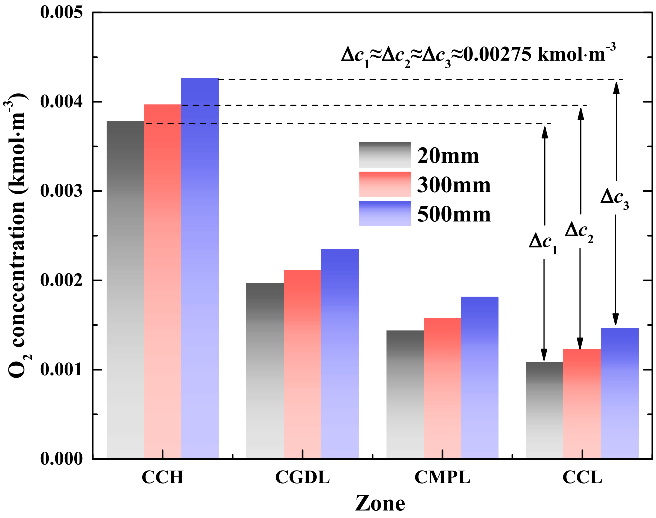

Fig. 8. O_2 concentration in the cathode.

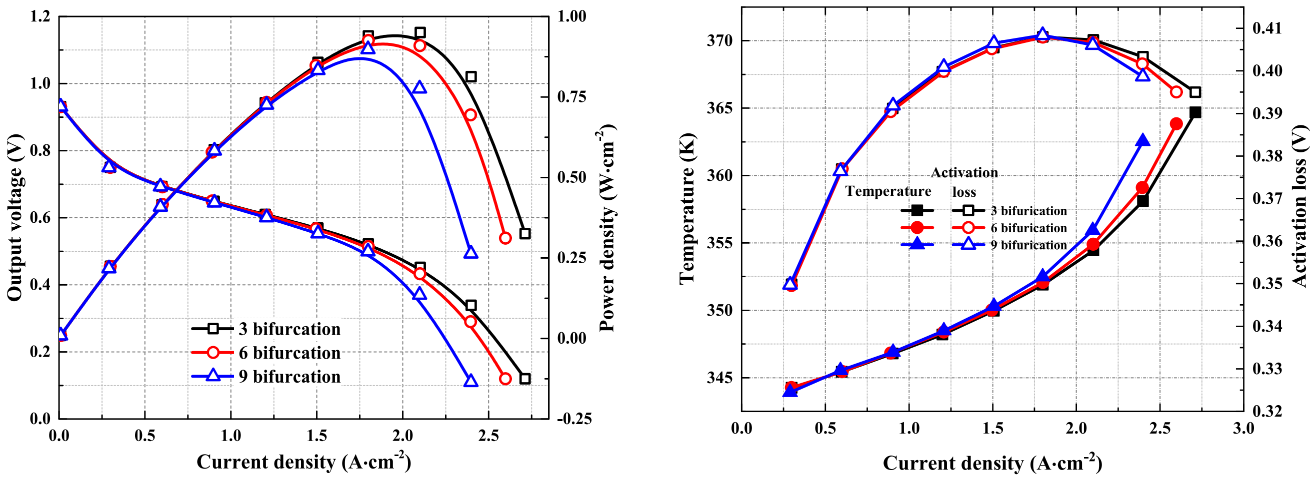

(a) Polarization and power density curve

(b) Activation loss

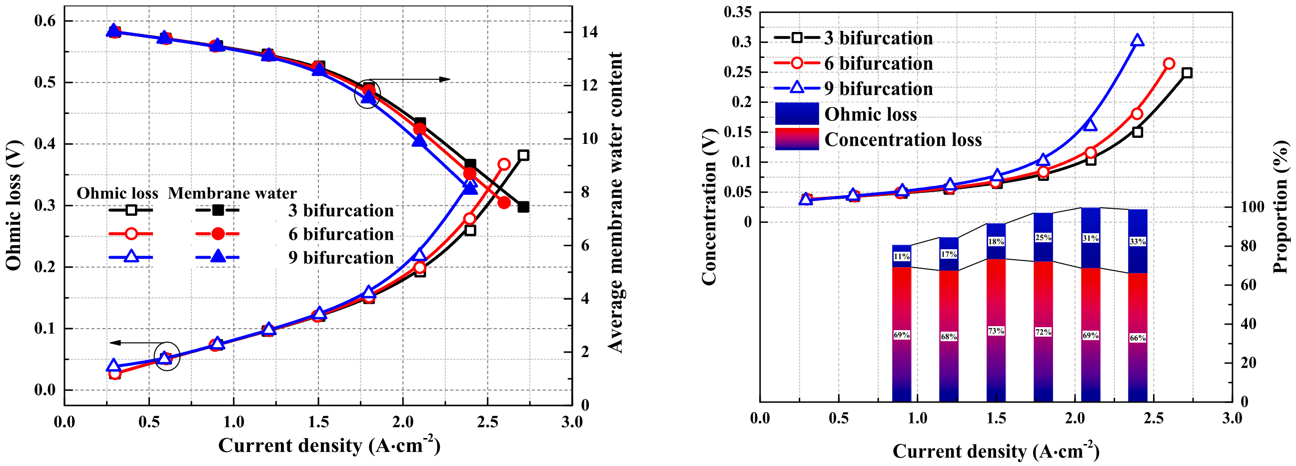

(c) Ohmic loss

(d) Concentration loss

Fig. 9. Effect of branch number on PEMFC performance and voltage loss.

corresponding to varying numbers of channel branches. With an increase in the number of branches, a gradual decline in performance is observed, as shown in Fig. 9(a). At 2.1 $\mathrm{A\cdot cm^{-2}}$, the performance of 9-branch and 6-branch is 4.3 % and 18.3 % lower than that of 3-branch, respectively. The rise in concentration loss and ohmic loss primarily contributed to the performance decline, as shown in Fig. 9(d). The subsequent section offers an analysis of the three types of losses.

As shown in Fig. 9(b), the change in the activation loss is small for the three branch numbers. Only in the region of high current density, some differences are caused by different temperatures. The activation losses are almost identical at the same temperature. A flow-field plate with a large number of branches has a low energy-conversion efficiency. Under a high current, more heat is generated, and the temperature is high, thereby reducing the activation loss.

The difference in ohmic loss is also temperature-dependent. High temperatures lead to dehydration of the inner membrane of the proton-exchange membrane, resulting in elevated proton conduction resistance, as shown in Fig. 9(c). At 2.1 $\mathrm{A\cdot cm^{-2}}$, the ohmic losses for the 6 and 9 branches exceed those of the 3 branches by approximately 3.5 % and 13.2 %, respectively.

The primary factor influencing performance variation at high current density is concentration loss (refer to Fig. 9(d)). Fig. 10(a) illustrates that similar to Section 3.1, the mass transfer resistance from the channel to the catalyst layer is comparable in all three cases ($\Delta c_1 = \Delta c_2 = \Delta c_3$). Discrepancies in bulk concentration result in varying concentration losses. As shown in Fig. 10(b), the reactant concentration distribution at the CGDL/CMPL interface reveals significant unevenness between channels. An increase in branch numbers leads to a noticeable concentration trough in the central region.

The reactants were sequentially distributed from the inlet to each parallel channel; therefore, the reactant concentration in each channel closely correlated with the fluid distribution. Fig. 10(c) shows the velocity distribution in the channel, indicating flow distribution unevenness. For instance, with 3 branches, the third channel near the outlet exhibited a high flow rate. In the case of 9 branches, the channel flow rates from high to low were as follows: closest to the outlet side channel, closest to the inlet side channel, and the middle area channel. A comparison between Fig. 10(b) and Fig. 10(c) reveals that the reactant concentration in the high flow rate channel area is also high. Consequently, the uneven reactant concentration results from irregular flow distribution. An increase in the number of branches causes uneven flow distribution, leading to local gas shortages and a subsequent decrease in

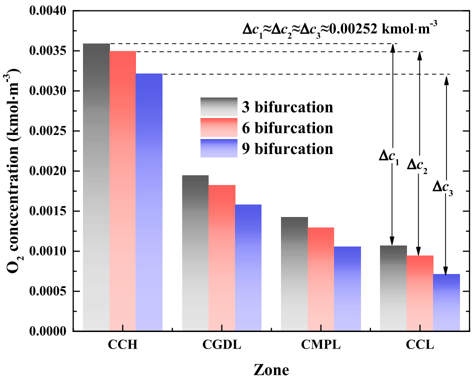

(a) Average O_2 concentration in cathode

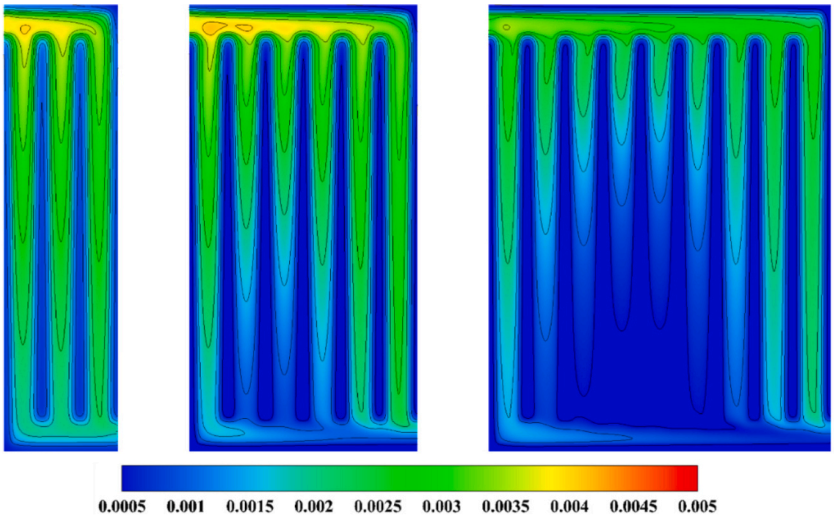

(b) O_2 concentration distribution at the interface of CGDL/CMPL

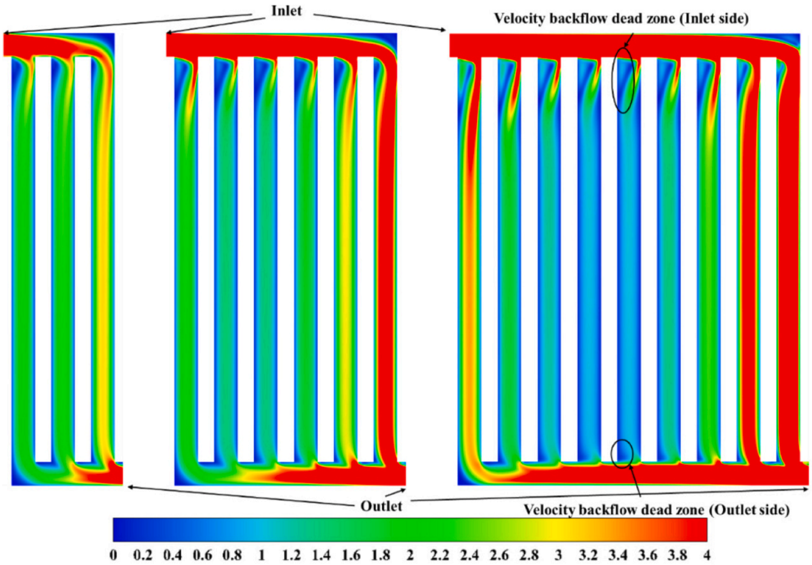

(c) Velocity magnitude

Fig. 10. Effect of branch O_2 concentration distribution and velocity magnitude.

average reactant concentration.

Fig. B4 in Appendix B illustrates the pressure drop variation in the cathode and anode channels. An increase in the number of branches raises the local resistance, corresponding to the channel turning. Fig. 10 (c) depicts a dead zone of velocity backflow at the junctions of the inlet, outlet, and parallel flow channels. At 2.1 A·cm^{-2}, the cathode side pressure drop of 6 and 9 branches is 2.4 and 4.4 times that of 3 branches, respectively.

3.3. Proportional amplification

Two scaling factors, 1.5 and 2, were modeled in this study. Fig. 11(a) shows the performance curve post-proportional scaling. It is evident that a simple scaled flow-field plate leads to a rapid decline in performance, with a significant deterioration across all current density levels. For instance, at 2.1 A·cm^{-2}, the power density with 1.5- and 2-times magnification is 42.6 % and 75.6 % lower than the original, respectively. Fig. 11(b), (c), and (d) demonstrate the substantial impact of scaling up on the three losses. Notably, the trend of activation loss differs from the other two types of losses. Proportional amplification aids in reducing activation loss, but exacerbates the other two losses. The histogram in Fig. 11(d) shows the contributions of ohmic and concentration losses. The three types of losses, from highest to lowest, comprise ohmic loss, concentration loss, and activation loss.

In Fig. 11(b), temperature significantly influences the activation loss. Proportional amplification causes performance degradation, leading to increased heat generation that elevates the temperature, thereby aiding in reducing the activation loss to some extent. At 2.1 A·cm^{-2}, the activation loss decreased by 0.023 V compared to the original value when amplified by a factor of 2. The temperature range associated with the maximum activation loss point was 350–352 K.

Fig. 11(c) shows that the increase in ohmic loss due to the increase in temperature is much larger than the decrease in activation loss. At 2.1 A·cm^{-2}, ohmic loss increased by 0.192 V, surpassing the reduction in activation loss by a factor of 8.4. The membrane water content variation curve suggests that proton conduction loss constituted the primary contributor to ohmic loss.

As shown in Fig. 11(d), scaling up results in a rise in concentration loss. As shown in Fig. 12(a), $\Delta c_1 < \Delta c_2 < \Delta c_3$; that is, the mass transfer deteriorated to a certain extent due to the amplification of the scale. When the flow field is enlarged at n scale, the reactant transport distance under the rib is increased by n times. Therefore, the concentration of reactants under the rib will be significantly reduced. At the same time, the bulk concentration also decreases after scaling up, as shown in Fig. 12(a). After zooming three to the same viewing angle, as shown in Fig. 12(b), the O_2 concentration in the porous electrode decreased

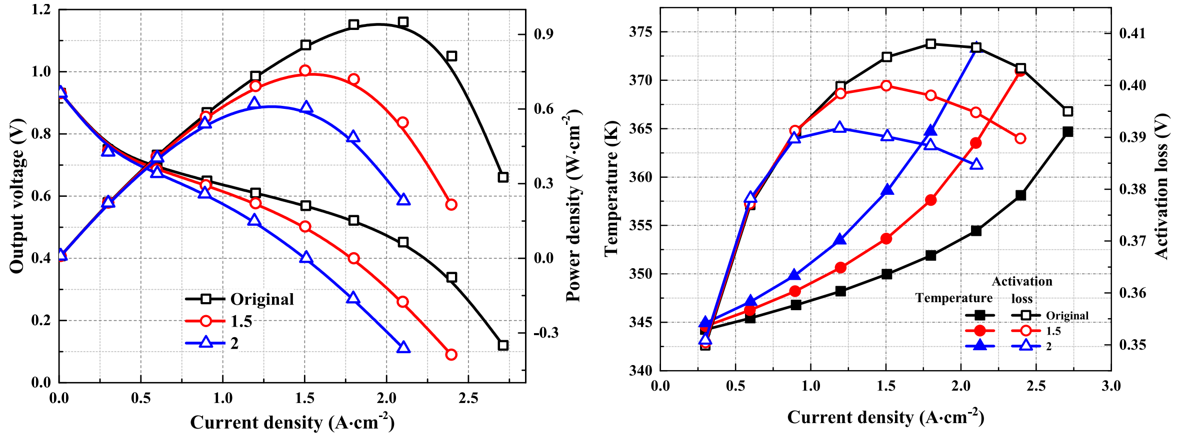

(a) Polarization and power density curve

(b) Activation loss

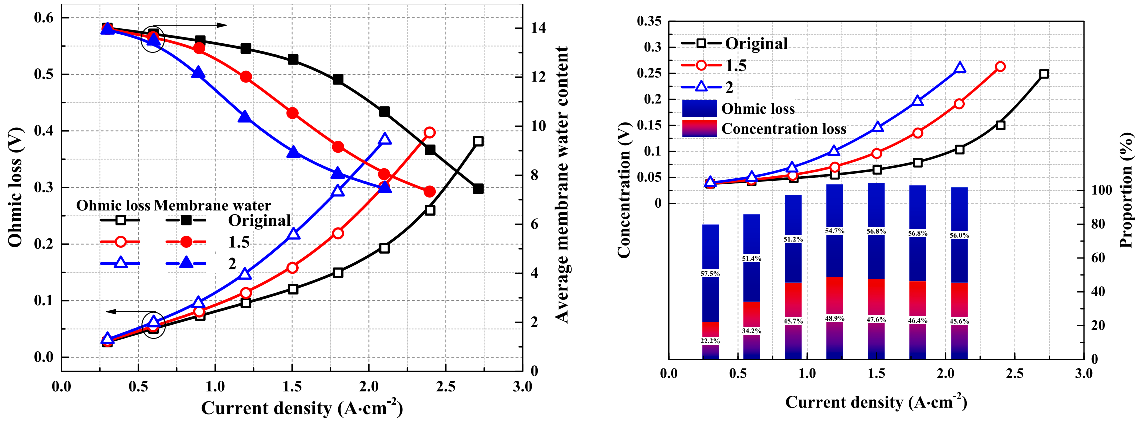

(c) Ohmic loss

(d) Concentration loss

Fig. 11. Effect of proportional amplification on PEMFC performance and voltage loss.

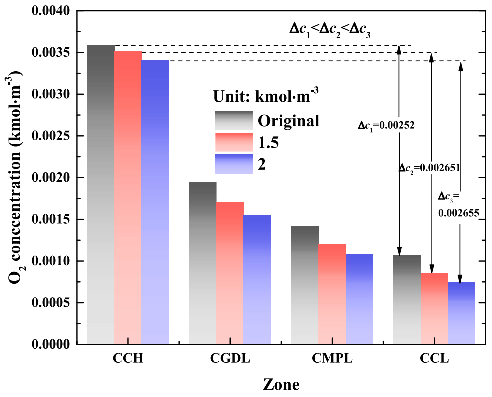

(a) Average O_2 concentration at the cathode

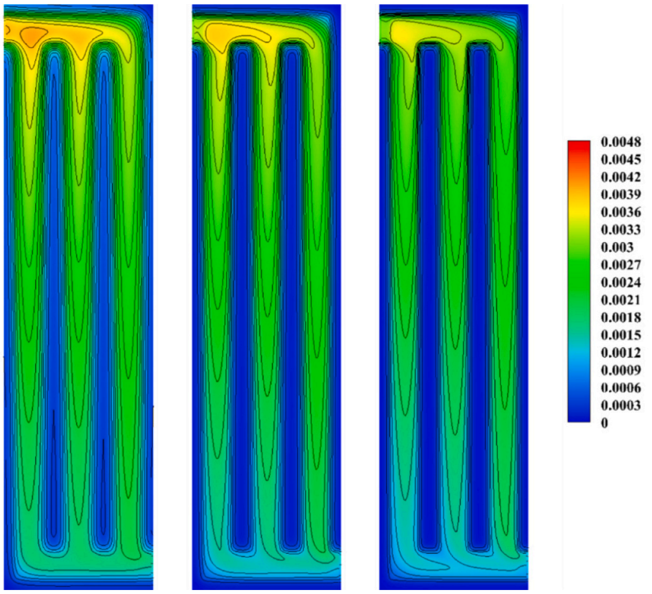

(b) O_2 concentration at the porous electrode

Fig. 12. O_2 concentration statistics distribution under different scaling factors.

significantly, especially in the rib region. The area under the rib accounted for 39.2 % of the total reaction area; therefore, the lack of reactants in this area significantly increased the total overpotential.

As depicted in Fig. B5 in Appendix B, the pressure drop escalates with scaling up. At 2.1 $A\cdot cm^{-2}$, the pressure drop on the cathode side at 1.5 and 2 times magnification is 2.0 and 3.4 times that of the original flow field, respectively. Assuming a scale factor of n, the inlet flow rate and flow distance increase by n times, resulting in a proportional expansion of the pressure drop by approximately n^2 times.

3.4. *Effect of C/R ratio*

Three C/R ratios, 10:7, 1:1, and 7:10, were simulated in the present study. Fig. 13(a) shows that an increase in the C/R ratio led to a gradual improvement in output performance, particularly noticeable at medium and high current densies. The three voltage losses are analyzed respectively in Fig. 13(b), (c), and (d).

According to the contribution factor shown in Fig. 13(d), within the range of 0–2.1 $A\cdot cm^{-2}$, concentration loss remains the primary cause of performance variation (contribution factor approaching or exceeding 90 %). Conversely, there was no notable disparity in activation and concentration losses across various C/R ratios. As shown in Fig. 13(b), the variation in activation loss for the same current density was below 0.015 V for the three C/R ratios.

The slight difference in activation loss primarily stems from temperature variations. The contact area between the rib and porous electrodevaries with the C/R ratios of the flow field plate, resulting in distinct heat dissipation capacities. Generally, wider ribs correspond to lower thermal resistance and enhanced heat dissipation. According to the curve of temperature versus current density, when the current density is less than 2.1 $A\cdot cm^{-2}$, the average temperature in CCM is the lowest in the working condition corresponding to C/R = 7:10. Consequently, this configuration yields the highest activation loss at a C/R ratio of 7:10. At 2.1 $A\cdot cm^{-2}$, the temperature for 10:7 exceeds that of 7:10 by 3 K, leading to a maximum activation loss difference of 0.015 V.

Regarding ohmic loss, Fig. 13(c) shows that at current densities below 2.1 $A\cdot cm^{-2}$, the ohmic loss remains largely unaffected by the C/R ratio. However, when the current density further increases (greater than 2.1 $A\cdot cm^{-2}$) due to the sharp degradation of performance under the condition of large C/R ratio (caused by concentration loss), the sudden increase of heat production will lead to the rise of temperature. It dehydrates the membrane and increase the internal resistance rapidly. Therefore, it can be observed in Fig. 13(c) that under high current, the smaller the C/R, the greater the ohmic loss.

Fig. 13(d) shows that the concentration loss contribution factor reaches 90 %. The concentration loss was minimal, and performance was optimal at C/R = 7:10 due to varying C/R structures that affected mass transfer capacity. It can be seen from Fig. 14(a) that under the three C/R ratios, the bulk concentrations of reactants in the channel were similar. However, reactant concentrations in the porous electrode were significantly different due to varying mass transfer abilities. Referring to the oxygen concentration distribution in Fig. B2(c), (d), (e) in Appendix B, it is evident that at C/R = 7:10, O_2 concentration in the porous electrode is notably low. Reactants traverse the channel, gas diffusion layer, microporous layer, and catalyst layer in the through-plane direction. By comparing reactant concentration differences in adjacent layers in Fig. 14(a), it can be inferred that the variance in mass transfer capacity primarily stems from the flow field plate to the GDL stage. Fig. 14(b) depicts the O_2 concentration variation at the GDL/MPL interface of the cathode in the X-direction. Solid symbols denote the flow channel area, while hollow symbols represent the rib area. Notably, at C/R = 7:10, reactant concentration beneath the channel and rib was low, peaking at C/R = 10:7. With an increase in the number of ribs, the path of reaction gas to the reaction area under the rib elongated, leading to a substantial rise in mass transfer resistance.

Fig. B6 in Appendix B shows the pressure drop variation in the cathode and anode channels. The pressure drops in both channels increase proportionally with the current density. The wider the channel, indicated by a higher channel/ridge width ratio, the lower the pressure drop. Specifically, the pressure drops for C/R = 7:10 and 1:1 rose by 40 % and 30 %, respectively, compared to 10:7. Consequently, it is essential to account for pump power loss when determining the C/R ratio in the design process.

3.5. *Comparison of different design strategies*

Area magnification is enhances PEMFC power but also increases pump loss. This trade-off is detailed in Sections 3.1 to 3.3. To compare design methods across different areas, power density is used to normalize the impact of area size. The pump and PEMFC power densities in various scenarios are considered as benefits and costs, respectively. From power curves shown in Figs. 7(a), 9(a), 11(a), it can be found that at a current density of approximately 2.1 $A\cdot cm^{-2}$, the power density reaches its peak value. In other words, the current density (2.1 $A\cdot cm^{-2}$)

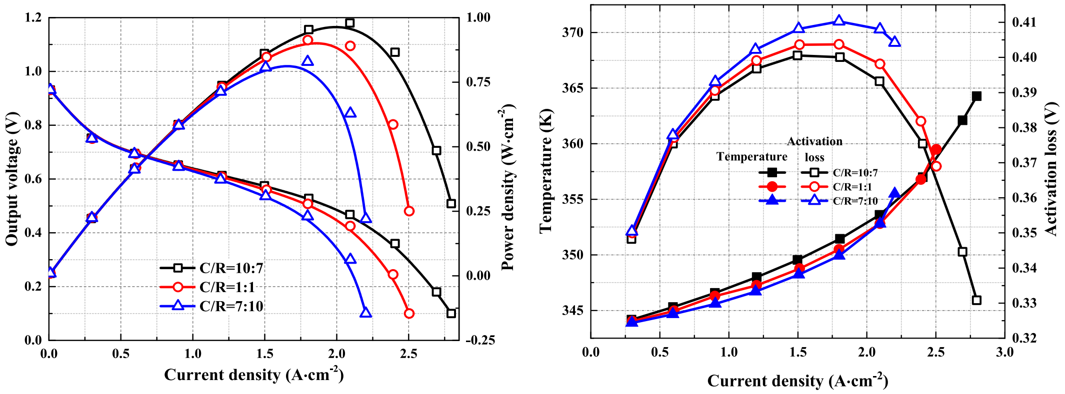

(a) Polarization and power density curve (b) Activation loss

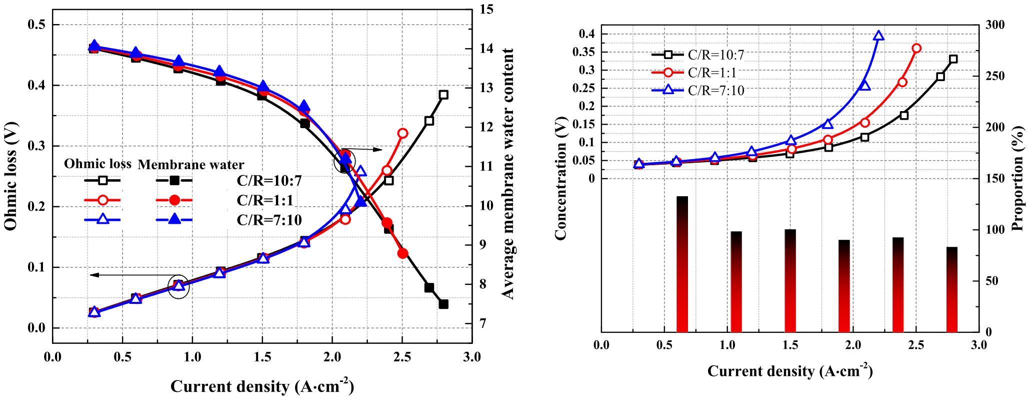

(c) Ohmic loss (c) Concentraion loss

Fig. 13. Effect of C/R ratio on PEMFC performance and voltage loss.

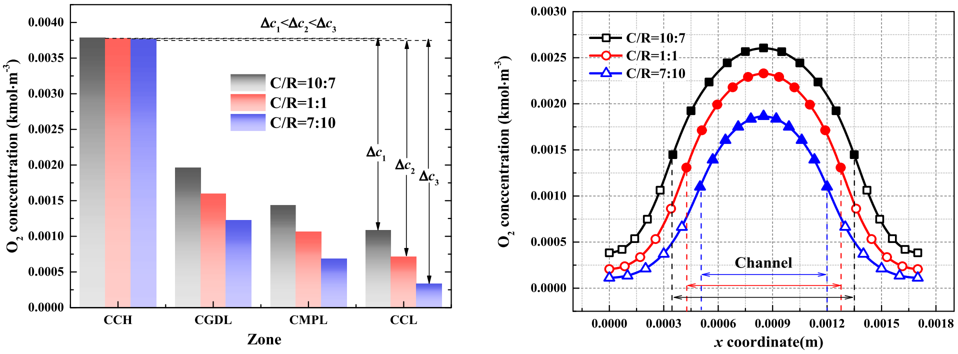

(a) Average O_2 concentration in cathode (b) O_2 concentration in *x* direction

Fig. 14. Analysis of O_2 concentration under different C/R ratio.

can be regarded as a representative point for high-power fuel cell application scenarios. Therefore, the pump power density of different cases under the same current density 2.1 A·cm^{-2} are compared. These comparisons are visually represented in a bubble color chart, as depicted in Fig. 15. Bubble size corresponds to PEMFC power density, with values marked. Different bubble colors denote various area-magnification strategies. The pump power density (P_{pump}) is calculated as follows:

$$P_{pump} = \frac{\Delta p q_v}{\xi A_{act}} \tag{20}$$

where Δp (Pa) is pressure drop; q_v (m^3·s^{-1}) is volume flow rate; $\xi = 0.7$ is compressor efficiency [23]; A_{act} (m^2) is active area.

Extending the channel length directly enlarges the active area without compromising the cell performance, albeiy with a significant

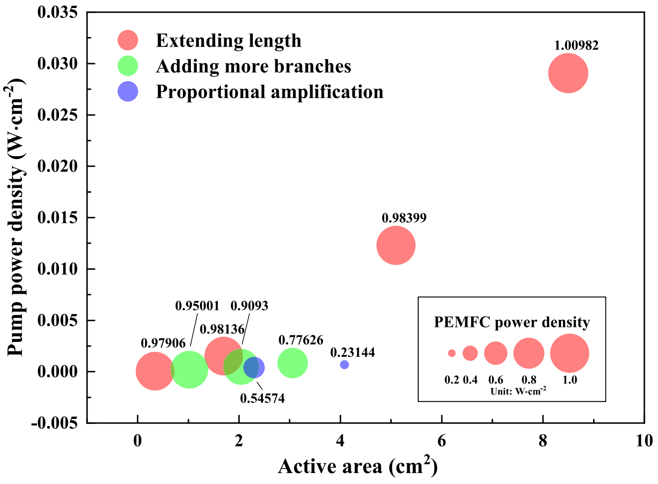

Fig. 15. Comparison of different strategies.

increase in pressure drop. Beyond 300 mm channel length, the pump power density escalates exponentially. Specifically, extending the channel from 100 mm to 300 mm results in an 8.2-fold increase in pump power density, primarily due to frictional resistance. It is mainly attributed to frictional resistance. When the flow channel is extended by n times, that is, when the active area (A_{act}) increases by n times, the pressure drop (Δp) will increase by n^2 times (explained below). The inlet flow rate (q_{v}) will increase by n times, then according to Eq. (20), the pump power density will increase by n^2 times. Higher air compressor power diminishes the net output power of the fuel cell system. Except for the 300 mm and 500 mm cases, pump power densities in other cases are notably smaller, approximately one order of magnitude lower than PEMFC power density, as shown in Fig. 15. Neither proportional amplification nor additional branches elevate pump power density. However, adopting proportional amplification significantly impairs the performance. For amplification factors of 1.5 and 2, PEMFC power density decreases by 42.6 % and 75.6 %, respectively. Conversely, increasing the number of branches minimizes performance degradation. PEMFC power densities with six and nine branches are 4.3 % and 18.3 % lower, respectively, than those with three branches, making it an effective flow-field design strategy for expanding the reaction area.

The three voltage losses were attributed to the final PEMFC performance under different designs. Based on the analysis in Sections 3.1 to 3.4, Table VI further summarizes the main factors for performance difference under different design strategies. It can be seen that concentration loss is the most important factor in the performance change in various structural design schemes. This reflects the key role of the flow-field plate in the transport of the reactants and products. When changing the channel length and C/R ratio, the concentration loss was the dominant reason for the performance difference, where the concentration loss contribution factor was more than 80 %, significantly higher than the other two voltage losses. In the two strategies of changing the number of branches and proportional amplification, the change in the ohmic or activation loss cannot be ignored. Elevated temperatures results in lower water contents in the membrane and higher ohmic losses. Each loss may change in different directions; for example, the activation loss increases, but the ohmic and concentration losses decrease when the PEMFC is proportionally enlarged. Furthermore, the specific reasons for the change in concentration loss are summarized. Changing the length of the channel and the number of branches alters the bulk concentration, whereas changing the C/R ratio mainly affects the mass transfer ability from the channel to the catalyst layer. Proportional amplification affects both simultaneously.

Table VI
Comparison of different design strategies.

Method	Activation loss	Ohmic loss	Concentration loss	Source of concentration loss
Change channel length	–	–	☆	Bulk concentration
Change sub-channel number	–	☆	☆	Bulk concentration
Proportional amplification	☆	☆	☆	Mass transport and bulk concentration
Change C/R ratio	–	–	☆	Mass transport

In addition to analyzing the electrical performance, we investigated the liquid water accumulation under various design strategies using the findings from a 3D two-phase simulation. Fig. B7(a) in Appendix B illustrates that as the channel length increases, the liquid water saturation in the porous electrode rises at high current densities. Correspondingly, at a high current density, a longer channel length results in lower temperature (Fig. 7(b)) due to reduced evaporation, leading to higher liquid water saturation. In Fig. B7(b), the liquid water content decreases with an increase in branch number, reflecting performance degradation and increased heat generation. This is consistent with the trend observed in membrane water (Fig. 9(c)). Fig. B7(c) shows the effect of the C/R ratio: a decrease in the C/R ratio, indicating a wider rib, hinders water discharge, thereby increasing liquid water saturation in the porous electrode. Regarding proportional amplification (Fig. B7(d)), liquid water accumulates at low current densities after scaling up, attributed to the longer drainage path resulting from a larger rib width. At high current densities, performance degradation leads to significant heat generation (refer to temperature in Fig. 11(b)), promoting water evaporation and consequently reducing liquid water saturation. In conclusion, increasing the branch number or the C/R ratio is advisable to mitigate liquid accumulation.

4. Conclusion

This study elucidated the impact of various area magnification strategies on cell performance. A method for extracting concentration losses was developed to compare and analyze the relative contributions of the three voltage losses to output performance changes. Considering the loss of pump power and change in performance, a strategy for area enlargement was proposed. These results are significant for the design of large-flow fields. Based on the analysis in this article, in the design of mainstream zone of large-area flow fields, area magnification should not be achieved simply by extending channel length, but different design strategies should be combined with different design strategies. By increasing the number of channel branches, the rapid increase in pump power loss can be avoided as much as possible. Besides, the strategy of proportional amplification (i.e. fixed C/R ratio) should not be adopted. And the C/R ratio should be increased to reduce the accumulation of water in the porous electrode and prevent water flooding. The main findings of this study are as follows:

(1) When designing a large-scale flow field based on typical units, the cell performance variation should be carefully considered. Both adding channel branches and proportional amplification lead to a performance decline, while extending channel length can slightly improve the PEMFC power density.

(2) Among three area manification strategies, adding channel branches is suggested, considering both pump loss and performance degradation. When the channel length was greater than 100 mm, the pump power density increased exponentially (more than eight times), which was unfavorable. Proportional amplification may cause a severe decline (> 40 %) in cell output performance.

(3) When the channel length and C/R ratio are changed, the concentration loss is the dominant reason for the performance difference, where the concentration loss contribution factor is more than 80 %, which is significantly higher than the other two voltage losses. However, in the other two strategies of changing the number of branches and proportional amplification, the ohmic or activation loss is also important.

(4) All three area magnification methods influenced the bulk concentration in the channel, thereby affecting the concentration loss. Moreover, proportional amplification and increasing C/R ratio can exacerbate the mass transport ability from the channel to theporous electrode, leading to increased concentration loss.

(5) After determining the catalyst material, the activation loss was significantly affected by the local temperature. An increase in temperature results in a decrease in activation loss. The ohmic loss is primarily dictated by the variation in membrane conductivity due to the membrane water content, which is also related to the temperature.

5. Future research needs

It is worth pointing out that further in-depth researches are needed in the future, and they can be indicated as follows: (1) Considering the effects of "contact resistance" and "GDL compression level" in the design of flow field. (2) Applying weight factors to compare different design strategies under the same active area. (3) Analyzing the effect of operating condition, like inlet humidty on simulation results. (4) Performing the non-steady simulation to consider transient effect.

CRediT authorship contribution statement

Zhuo Zhang: Writing – original draft, Software, Methodology, Investigation, Conceptualization. **Hong-Bing Quan:** Validation, Software. **Sai-Jie Cai:** Validation, Data curation. **Zheng-Dao Li:** Validation. **Wen-Quan Tao:** Writing – review & editing, Supervision.

Declaration of competing interest

The authors declare that they have no known competing financial interests or personal relationships that could have appeared to influence the work reported in this paper.

Acknowledgment

The study is supported by the projects of the Postdoctoral Innovation Talent Support Program (BX20240285M).

Appendix A. Supplementary data

Supplementary data to this article can be found online at https://doi.org/10.1016/j.apenergy.2025.125628.

Appendix B

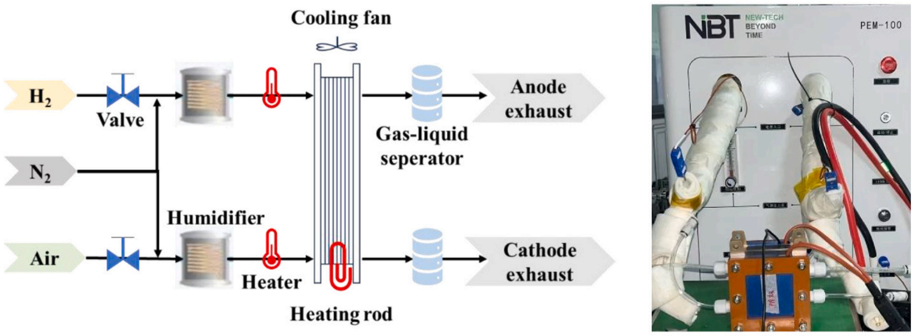

(a) Schematic diagram of test bench

(b) Experiment bench

Fig. B1. Experiment setup.

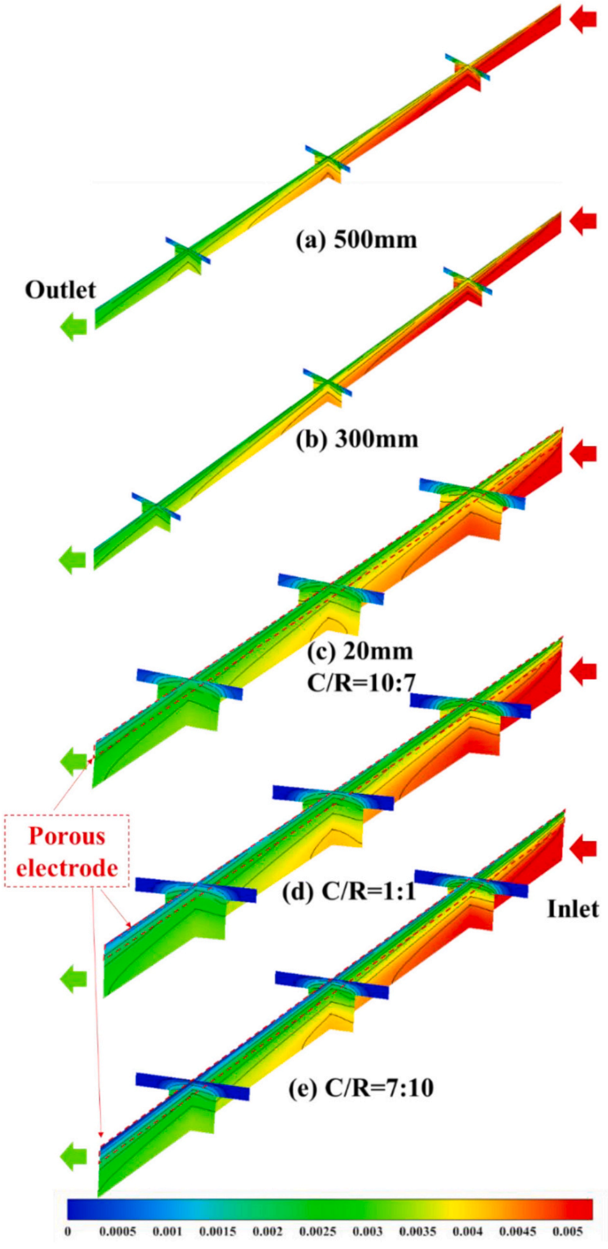

Fig. B2. O_2 concentration under different length and C/R ratio.

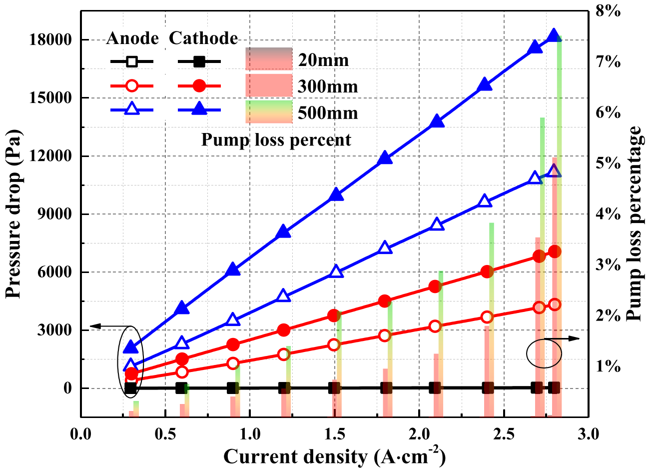

Fig. B3. Pressure drop and pump proportion under different channel length.

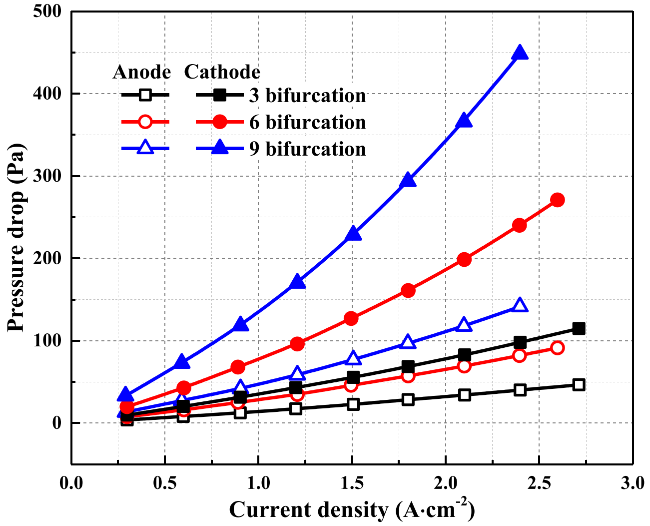

Fig. B4. Effect of branch number on pressure drop.

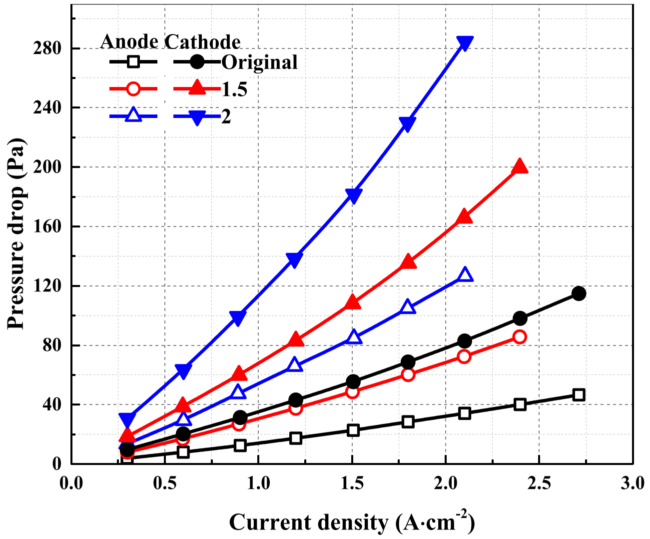

Fig. B5. Pressure drop under different scaling factors.

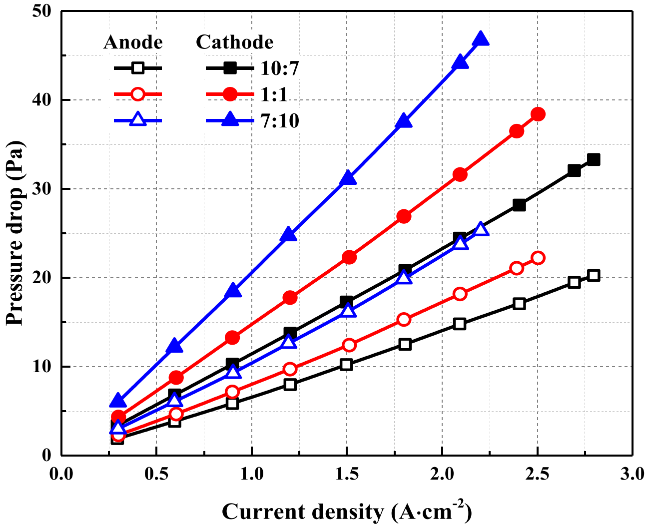

Fig. B6. Pressure drop under different C/R ratio.

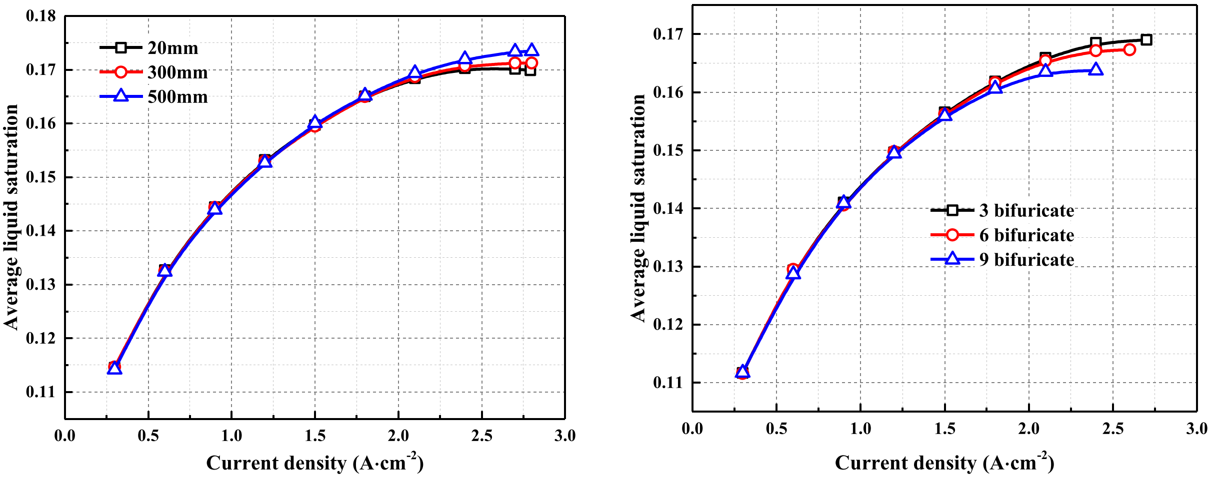

(a) Effect of channel length

(b) Effect of branch number

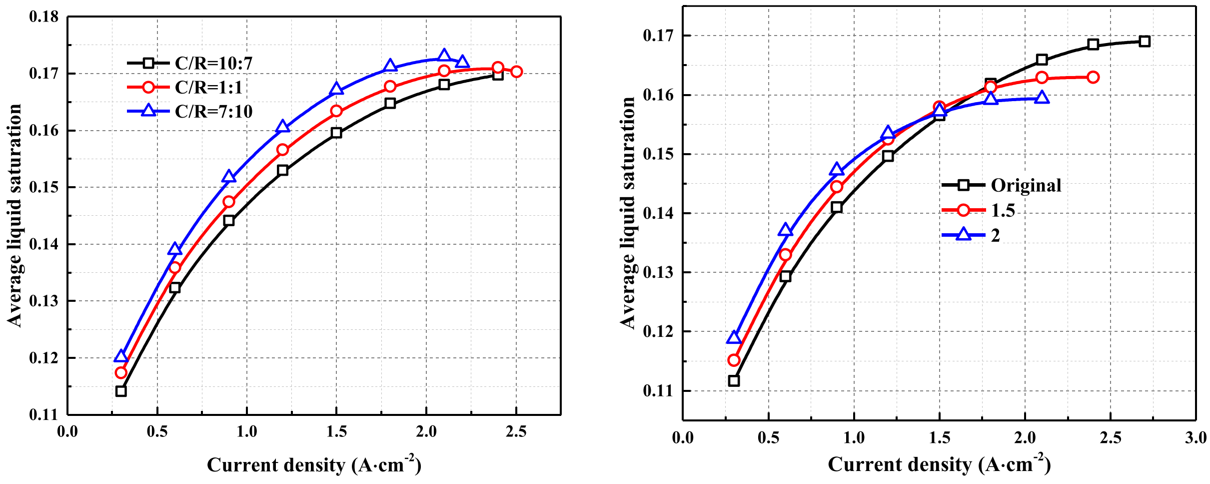

(c) Effect of channel/rib ratio

(d) Effect of scaling factors

Fig. B7. Liquid accumulation.

Appendix C

According to the formula for pressure drop of inner flow in microchannel,

$$\Delta p = f\frac{L}{D}\frac{\rho v^2}{2} \tag{C1}$$

where f is the friction factor, L (m) is the channel length, D (m) is the diameter, ρ (kg·m^{-3}) is the fluid density, v (m·s^{-1}) is the velocity flowing through the pipe. When Reynold number, Re, is low ($\langle$2000), the friction factor f can be calculated as [64]:

$$f = \frac{64}{Re} \tag{C2}$$

Substitute Eq. (C2) into Eq. (C1), then,

$$\Delta p = 32\frac{\eta L v}{D^2} \tag{C3}$$

When the flow channel is extended by n times, the inlet mass flow rate will increases proportionally by n times. That means both the velocity (v) and channel length (L) increases by n times. Then the pressure drop (Δp) will increase by n^2 times.

Data availability

Data will be made available on request.

References

[1] Zhou Y, Meng K, Liu W, Chen K, Chen W, Zhang N, et al. Multi-objective optimization of comprehensive performance enhancement for proton exchange membrane fuel cell based on machine learning. Renew Energy 2024;232:121126.

[2] Ye L, Qiu D, Peng L, Lai X. Conduction mechanism analysis and modeling of different gas diffusion layers for PEMFC to improve their bulk conductivities via microstructure design. Appl Energy 2024;362:122987.

[3] Fan LX, Tu ZK, Chan SH. Recent development of hydrogen and fuel cell technologies: a review. Energy Rep 2021;7:8421–46.

[4] Ma H, Liu J, Liang W, Li J, Zhao W, Sun P, et al. Effects of PEMFC cooling channel insulation coating on heat transfer and electrical discharge characteristics of nanofluid coolants. Appl Energy 2024;357:122514.

[5] Quan S, He H, Chen J, Zhang Z, Han R, Wang Y-X. Health-aware model predictive energy management for fuel cell electric vehicle based on hybrid modeling method. Energy 2023;278:127919.

[6] Li S, Djilali N, Rosen MA, Crawford C, Sui PC. Transition of heavy-duty trucks from diesel to hydrogen fuel cells: opportunities, challenges, and recommendations. Int J Energy Res 2022;46:11718–29.

[7] Meng H, Yu X, Luo X, Tu Z. Modelling and operation characteristics of air-cooled PEMFC with metallic bipolar plate used in unmanned aerial vehicle. Energy 2024;300:131559.

[8] Shahverdian MH, Sohani A, Zamani Pedram M, Sayyaadi H. An optimal strategy for application of photovoltaic-wind turbine with PEMEC-PEMFC hydrogen storage system based on techno-economic, environmental, and availability indicators. J Clean Prod 2023;384:135499.

[9] Liu Z, Shi M, Mohammadi MH, Luo H, Yang X, Babaei M. An improved capacitance–resistance model for analysing hydrogen production with geothermal energy utilisation. Int J Hydrog Energy 2024. https://doi.org/10.1016/j.ijhydene.2024.08.205. In press.

[10] Guan D, Pan B, Chen Z, Li J, Shen H, Pang H. Quantitative modeling and bio-inspired optimization the clamping load on the bipolar plate in PEMFC. Energy 2023;263:125951.

[11] Carral C, Mélé P. A numerical analysis of PEMFC stack assembly through a 3D finite element model. Int J Hydrog Energy 2014;39:4516–30.

[12] Su G, Yang D, Xiao Q, Dai H, Zhang C. Effects of vortexes in feed header on air flow distribution of PEMFC stack: CFD simulation and optimization for better uniformity. Renew Energy 2021;173:498–506.

[13] Cai F, Cai S, Tu Z. Proton exchange membrane fuel cell (PEMFC) operation in high current density (HCD): problem, progress and perspective. Energy Convers Manag 2024;307:118348.

[14] Zhang Z, Cai S-J, Li Z-D, Tao W-Q. Electrical and thermal performance analysis of PEMFC with coolant flow field under steady-state condition. Energy 2024;306:132288.

[15] Yin B, Xu S, Yang S, Dong F. Influence of microelliptical groove gas diffusion layer (GDL) on transport behavior of proton exchange membrane fuel cell (PEMFC). Int J Heat Mass Transf 2021;180:121793.

[16] Gao Y, Qu W, Zhu R. The impact of structural characteristics of the catalyst layer on fuel cell performance based on reconstruction method. J Power Sources 2021;482:228917.

[17] Liu X, Zhang J, Zheng C, Xue J, Huang T, Yin Y, et al. Oriented proton-conductive nano-sponge-facilitated polymer electrolyte membranes. Energy Environ Sci 2020;13:297–309.

[18] Zheng Z, Wang C, Chen C, Lin H, Zhang Z. Numerical study of hydrothermal and flow characteristics of PEMFC folded porous cathode flow field. Int J Hydrog Energy 2024;72:861–77.

[19] Zhang G, Qu Z, Tao W-Q, Wang X, Wu L, Wu S, et al. Porous flow field for next-generation proton exchange membrane fuel cells: materials, characterization, design, and challenges. Chem Rev 2023;123:989–1039.

[20] Chen X, Yu Z, Yang C, Chen Y, Jin C, Ding Y, et al. Performance investigation on a novel 3D wave flow channel design for PEMFC. Int J Hydrog Energy 2020;46:11127–39.

[21] Zhang G, Xie B, Bao Z, Niu Z, Jiao K. Multi-phase simulation of proton exchange membrane fuel cell with 3D fine mesh flow field. Int J Energy Res 2018;42:4697–709.

[22] Zhou Y, Chen B, Meng K, Zhou H, Chen W, Zhang N, et al. Optimal design of a cathode flow field for performance enhancement of PEM fuel cell. Appl Energy 2023;343:121226.

[23] Zhang S, Liu S, Xu H, Liu G, Wang K. Performance of proton exchange membrane fuel cells with honeycomb-like flow channel design. Energy 2022;239:122102.

[24] Rahmani E, Moradi T, Ghandehariun S, Naterer GF, Ranjbar A. Enhanced mass transfer and water discharge in a proton exchange membrane fuel cell with a raccoon channel flow field. Energy 2023;264:126115.

[25] Zhang Y, He S, Jiang X, Xiong M, Ye Y, Yang X. Three-dimensional multi-phase simulation of different flow fields with cooling channel in proton exchange membrane fuel cell. Int J Hydrog Energy 2022;47:37929–44.

[26] Nguyen BH, Kim HC. Numerical investigation of in-line and staggered trap channels in the serpentine flow field of PEMFCs. Int J Precis Eng Manuf-Green Technol 2024;122:591–606.

[27] Zhang Z, Bai F, He P, Li Z, Tao W-Q. A novel cathode flow field for PEMFC and its performance analysis. Int J Hydrog Energy 2023;48:24459–80.

[28] Wang N, Qu Z, Zhang G, Tang Z, Wang Y. Cross flow and distribution characteristics in automobile polymer electrolyte membrane fuel cells: a three-dimensional full-scale modeling study. J Power Sources 2023;580:233348.

[29] Zhang Z, Wang Q-Y, Bai F, Chen L, Tao W-q. Performance simulation and key parameters in-plane distribution analysis of a commercial-size PEMFC. Energy 2023;263:125897.

[30] Yu Y, Zhan Z, He L, Yang X, Wan X, Sui P-C, et al. Effects of distribution zone design on flow uniformity and pressure drop in PEMFC. J Electrochem Soc 2021;168:094505.

[31] Lu W, Pan W, Chen Z, Gao Y, Ding L, Chen X, et al. Structural optimization of distribution zone for large-sized PEMFC with high power density. Chem Eng Sci 2023;276:118803.

[32] Pan W, Wang B, Tang L, Gao Y, Ding L, Dai Z, et al. A novel design of distribution zone in scaled-up PEM fuel cells based on active control of transverse flow. AIChE J 2023;69:18178.

[33] Min C, He J, Wang K, Xie L, Yang X. A comprehensive analysis of secondary flow effects on the performance of PEMFCs with modified serpentine flow fields. Energy Convers Manag 2019;180:1217–24.

[34] Santamaria AD, Cooper NJ, Becton MK, Park JW. Effect of channel length on interdigitated flow-field PEMFC performance: a computational and experimental study. Int J Hydrog Energy 2013;38:16253–63.

[35] Zou Y, Hua S, Wu H, Chen C, Wei Z, Hu Z, et al. Design of a new single-cell flow field based on the multi-physical coupling simulation for PEMFC durability. Energies 2023;16:5932.

[36] Yin C, Song Y, Liu M, Gao Y, Li K, Qiao Z, et al. Investigation of proton exchange membrane fuel cell stack with inversely phased wavy flow field design. Appl Energy 2022;305:117893.

[37] Zhang Y, He S, Jiang X, Ye Y, Xiong M, Yang X. Characteristics of proton exchange membrane fuel cell considering "dot matrix" gas distribution zones and waveform staggered flow field with cooling channels. Energy Convers Manag 2022;267:115881.

[38] Zhou Y, Lohan DJ, Zhou F, Nomura T, Dede EM. Inverse design of microreactor flow fields through anisotropic porous media optimization and dehomogenization. Chem Eng J 2022;435:134587.

[39] Rocha C, Knöri T, Ribeirinha P, Gazdzicki P. A review on flow field design for proton exchange membrane fuel cells: challenges to increase the active area for MW applications. Renew Sust Energ Rev 2024;192:114198.

[40] Fan L, Tu Z, Chan SH. Recent development in design a state-of-art proton exchange membrane fuel cell from stack to system: theory, integration and prospective. Int J Hydrog Energy 2023;48:7828–65.

[41] Reshetenko T, Polevaya O. Determination of oxygen mass transport resistance in proton exchange membrane fuel cells with an open flow field architecture. Electrochim Acta 2021;387:138529.

[42] Xia Z, Chen H, Zhang T, Pei P. Effect of channel-rib width ratio and relative humidity on performance of a single serpentine PEMFC based on electrochemical impedance spectroscopy. Int J Hydrog Energy 2022;47:13076–86.

[43] Yuan H, Dai H, Ming P, Zhao L, Tang W, Wei X. Understanding dynamic behavior of proton exchange membrane fuel cell in the view of internal dynamics based on impedance. Chem Eng J 2022;431:134035.

[44] Ma T, Zhang Z, Lin W, Cong M, Yang Y. Impedance prediction model based on convolutional neural networks methodology for proton exchange membrane fuel cell. Int J Hydrog Energy 2021;46:18534–45.

[45] Lim IS, Lee YI, Kang B, Park JY, Kim MS. Electrochemical performance and water management investigation of polymer electrolyte membrane fuel cell (PEMFC) using gas diffusion layer with polytetrafluoroethylene (PTFE) content gradients in through-plane direction. Electrochim Acta 2022;421:140509.

[46] Lu G, Liu M, Su X, Zheng T, Luan Y, Fan W, et al. Study on counter-flow mass transfer characteristics and performance optimization of commercial large-scale proton exchange membrane fuel cells. Appl Energy 2024;359:122743.

[47] Xie B, Zhang H, Huo W, Wang R, Zhu Y, Wu L, et al. Large-scale three-dimensional simulation of proton exchange membrane fuel cell considering detailed water transition mechanism. Appl Energy 2023;331:120469.

[48] Liu B, Huo W, Xie B, Gao Q, Bao Z, Li H, et al. Effects of sub-distribution zone structure of bipolar plate on the mass transport of large-area proton exchange membrane fuel cells. Int J Heat Mass Transf 2024;222:125169.

[49] Wu L, Zhang G, Shi X, Pan Z, Xie B, Huo W, et al. All-scale investigation of a commercial proton exchange membrane fuel cell with partially narrow channels. J Power Sources 2024;589:233779.

[50] Zhang G, Wu L, Tongsh C, Qu Z, Wu S, Xie B, et al. Structure design for ultrahigh power density proton exchange membrane fuel cell. Small Methods 2023:2201537.

[51] Zhang Y, He S, Jiang X, Wang Z, Yang X, Fang H, et al. Investigation on performance of full-scale proton exchange membrane fuel cell: porous foam flow field with integrated bipolar plate/gas diffusion layer. Energy 2024;287:129664.

[52] Bulgarini M, Della Torre A, Baricci A, Grimaldi A, Marocco L, Mereu R, et al. Computational fluid dynamic investigation of local flow-field conditions in lab polymer electrolyte membrane fuel cells to identify degradation stressors and performance enhancers. Energies 2024;17:3643.

[53] Yin C, Yang H, Liu Y, Wen X, Xie G, Wang R, et al. Numerical and experimental investigations on internal humidifying designs for proton exchange membrane fuel cell stack. Appl Energy 2023;348:121543.

[54] Wu L, Zhang G, Xie B, Huo W, Jiao K, An L. Elucidating the automobile proton exchange membrane fuel cell of innovative double-cell structure by full-morphology simulation. Int J Heat Mass Transf 2023;217:124666.

[55] Wan Z, Yan H, Sun Y, Yang C, Chen X, Kong X, et al. Thermal management improvement of air-cooled proton exchange membrane fuel cell by using metal foam flow field. Appl Energy 2023;333:120642.

[56] Shirong H, Mu X, Xiaohui J, Xi Y, Yuntao Y, Yong Z. Study on 3D simulation performance of large-scale proton exchange membrane fuel cell with distribution region. Energy Technol 2023:2201463.

[57] Park D, Ham S, Sohn Y-J, Choi Y-Y, Kim M. Mass transfer characteristics according to flow field and gas diffusion layer of a PEMFC metallic bipolar plate for stationary applications. Int J Hydrog Energy 2023;48:304–17.

[58] Cai Y, Yue S, Wei F, Hu J, Chen B. Research on performance of proton exchange membrane fuel cell with an innovative flow field. Case Stud Therm Eng 2023;50:103418.

[59] Hao J, Chen J, Ma T, Hao T, Zhou J, Du X. Flow channel structure optimization and analysis of proton exchange membrane fuel cell based on the finite data mapping and multi-field synergy principle. Int J Heat Mass Transf 2023;207:123997.

[60] Jing G, Hu C, Qin Y, Sun X, Ma T. Complex mechanisms of PEMFC performance variations influenced by both structural deformation and contact resistance under the clamping force. Int J Hydrog Energy 2024;58:137–48.

[61] Zhang Z, Tao W-Q. Effect of assembly pressure on the performance of proton exchange membrane fuel cell. Energy Storage Saving 2023;2:359–69.

[62] O'Hayre R, Cha SW. Fuel Cell Fundamentals, 3rd Edition. Canada: John Wiley & Sons, Inc., Hoboken, New Jersey.; 2016.

[63] Zhang Z, Shi J, Cheng X, Dai Y, Tao W. Numerical examination of high-pressure fuel injection in common rail injector based on hydro-mechanical model. Phys Fluids 2022;34:057114.

[64] Idel'Chik I. Handbook of hydraulic resistances [in Russian]. Moscow: Mashinostroenie; 1975.